Astronomy & Astrophysics manuscript no. output
March 10, 2026

Luminaries in the Sky: The TESS LEGACY Sample of Bright Stars

II. In-depth seismic characterisation of 32 naked-eye stars in the PLATO LOP fields

E. Panetier[1], G. T. Hookway[2], E. Corsaro[3], S. N. Breton[3], R. A. García[4], B. Liagre[1], M. N. Lund[5], M. B. Nielsen[2], D. B. Palakkatharappil[4], L. Debacker[4, 6], J. Gosmain[4, 7], M. Chaumard[8], A. Chontos[9], F. Grundahl[5], S. Mathur[10, 11], and A. R. G. Santos[4]

[1] Université Paris Cité, Université Paris-Saclay, CEA, CNRS, AIM, 91191, Gif-sur-Yvette, France
e-mail: `eva.panetier@cea.fr`
[2] School of Physics and Astronomy, University of Birmingham, Birmingham B15 2TT, UK
[3] INAF – Osservatorio Astrofisico di Catania, Via S. Sofia, 78, 95123 Catania, Italy
[4] Université Paris-Saclay, Université Paris Cité, CEA, CNRS, AIM, 91191, Gif-sur-Yvette, France
[5] Stellar Astrophysics Centre, Department of Physics and Astronomy, Aarhus University, Ny Munkegade 120, DK-8000 Aarhus C, Denmark
[6] IMT Atlantique, Technopole Brest-Iroise CS83818, 29238 Brest Cedex 03, France
[7] Institut Villebon - *Georges Charpak*, Université Paris-Saclay, 91400 Orsay, France
[8] Ecole Centrale-Supelec, Université Paris-Saclay, 91190 Gif-sur-Yvette, France
[9] Department of Physics and Astronomy, Dartmouth College, Hanover, NH USA
[10] Instituto de Astrofísica de Canarias (IAC), E-38205 La Laguna, Tenerife, Spain
[11] Universidad de La Laguna (ULL), Departamento de Astrofísica, E-38206 La Laguna, Tenerife, Spain

Received ; accepted

ABSTRACT

The Transiting Exoplanet Survey Satellite (TESS) is conducting a nearly full-sky survey, enabling the photometric characterisation of millions of stars. The forthcoming PLAnetary Transits and Oscillations of stars mission (PLATO) will provide long-duration, high-precision photometry of tens of thousands of bright stars to be characterised through asteroseismology. The TESS Luminaries Sample is a catalogue of 196 bright naked-eye ($V < 6$) main-sequence (MS) and sub-giant (SG) stars exhibiting solar-like oscillations Among them, the subset located within the PLATO Long-duration Observation Phase (LOP) fields constitutes an exceptional set of benchmark targets that will be observable by PLATO from the earliest phases of the mission, making them ideal calibrators during commissioning and the first months of science operations. This paper aims to provide an in-depth asteroseismic characterisation of 32 Luminaries stars that fall within the PLATO LOP fields of view. Individual mode parameters were extracted using three independent seismic pipelines, one of which was similar to the algorithms used in the official PLATO pipeline. The Peirce criterion and a Z-score were applied to select a reference dataset for each star, taking into account the observing cadence, the data calibration and the adopted pipeline. We analyse 32 MS and SG stars up to TESS Sector 88, with individual mode frequencies derived for the first time for 26 of them. For all stars, we derived large and small separations, the asymptotic phase term ε, radial mode amplitudes, and mean linewidths per order. Comparisons with previous *Kepler* observations reveal consistent trends in the seismic parameters, confirming the robustness of our analysis based on TESS data. In sub-giants, mixed-mode identification differs in the three pipelines, revealing extraction inconsistencies requiring longer datasets to improve our mode identifications. These results demonstrate the capability of TESS to deliver high-quality asteroseismic benchmarks for MS and SG stars. The Luminaries stars located in the PLATO LOP fields constitute a unique reference set that will play a crucial role in validating, calibrating, and optimising PLATO's seismic performance from the earliest stages of the mission.

1. Introduction

The PLAnetary Transits and Oscillations of stars (PLATO; Rauer et al. 2025) mission, scheduled for launch in January 2027, is designed to detect and characterise exoplanets through high-precision photometry. Its ultimate goal is the detection of terrestrial planets orbiting Sun-like stars, while also enabling a census of planetary systems around a broader range of solar-like stars, thereby contributing to our understanding of planetary system formation and evolution. A key aspect of its observing strategy is to focus on two dedicated regions of the sky, known as the Long-duration Observation Phase (LOP) fields, each covering an area of 49° × 49° (Rauer et al. 2025). According to the current mission plan, each LOP field will be monitored for approximately two years, although this may be revised following evaluation of initial observations. The mission is scheduled to begin observations in the southern LOP field, known as LOPS2 (Nascimbeni et al. 2025), and may subsequently continue at LOPN1, the current candidate field proposed by Nascimbeni et al. (2022) in the northern hemisphere.

PLATO will benefit from a careful characterisation of its instrumental performance and the robustness of its data reduction and analysis pipelines, particularly during commissioning and the early observing phases. In this context, well-characterised seismic benchmark stars within the LOP fields provide useful reference measurements. A comparison of the seismic results with previous determinations allows an assessment of the instrument performance as well as the reliability and internal consistency of the analysis pipelines.

A particularly valuable set of potential seismic calibrators has been identified within the Transiting Exoplanet Survey Satellite (TESS; Ricker et al. 2014) Luminaries Sample (TLS; Lund et al. 2025, hereafter Paper I). This sample consists of 196 bright ($V < 6$) main-sequence (MS) and sub-giant (SG) solar-like stars observed by TESS. Among them, 34 stars lie within the planned PLATO LOP fields and therefore represent prime seismic benchmarks for the mission. In the present study, we determine the detailed seismic properties of 32 of these targets, while 171 Pup and χ Dra are analysed in dedicated companion papers (Lund et al., in prep.; Rudrasingam et al., in prep.). These stars will play a key role in validating PLATO's early seismic performances.

The most precise asteroseismic constraints are obtained when individual oscillation mode frequencies are extracted. However, the feasibility and robustness of this extraction depend strongly on the stellar properties and evolutionary stage. F-like stars present particular challenges, as their oscillation modes exhibit large linewidths due to shorter mode lifetimes (Appourchaux et al. 2012a; Compton et al. 2019). The resulting broader and partially overlapping peaks complicate the identification of individual modes and reduce the precision of frequency determinations. Such stars occupy the upper boundary of the MS region of the Hertzsprung–Russell diagram where solar-like oscillations are observed ($T_{\rm eff} \lesssim 6400$ K, Appourchaux et al. 2012b; Breton et al. 2023). In contrast, cooler solar-like MS stars ($5000 \lesssim T_{\rm eff} \lesssim 6400$ K, Lund et al. 2017) generally display narrower modes that allow for more straightforward frequency extraction. As stars evolve toward the sub-giant phase, structural changes in the interior lead to the appearance of mixed modes (Beck et al. 2011; Benomar et al. 2013; Appourchaux 2020). These modes introduce additional complexity in the frequency spectrum and require dedicated identification strategies (e.g. Handberg et al. 2017; García Saravia Ortiz de Montellano et al. 2018; Themeßl et al. 2018; Kallinger 2019; Corsaro et al. 2020; Nielsen et al. 2021, 2025). However, they also provide powerful diagnostics of stellar interiors at this key evolutionary stage, as they probe both the deep core and the outer layers. This offers unique constraints on the internal structure (e.g. Deheuvels & Michel 2011; Bellinger et al. 2021; Buchele et al. 2025) and on angular momentum redistribution (e.g. Deheuvels et al. 2014, 2020; Buldgen et al. 2024), which remains one of the major open questions in stellar evolution. The sample of stars analysed in this work spans a range of effective temperatures and evolutionary stages across the main sequence and sub-giant branch. This diversity enables an evaluation of frequency extraction and mode identification under conditions representative of PLATO's future targets.

This paper is organised as follows. In Sect. 2, we describe the sample of stars, including a summary of the data calibration performed in Paper I and the additional calibration steps required for certain targets. Sect. 3 presents the three pipelines used for mode extraction. In Sect. 4, we report our peak-bagging results, beginning with the method used to select a reference dataset for each star, including the cadence and the analysis pipeline, and followed by a discussion of the results. Sect. 5 compares our findings with pre-existing studies. Finally, we summarise our findings in Sect. 6.

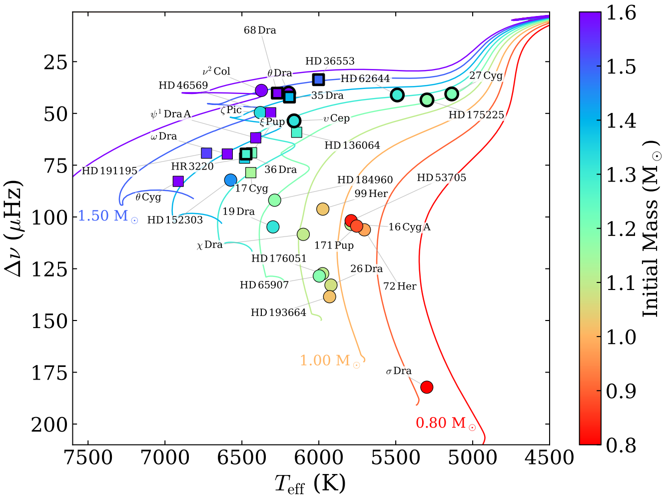

Fig. 1. HR diagram illustrating the relation between $\Delta\nu$ and $T_{\rm eff}$ for the sample of 34 TLS stars. The evolutionary tracks are taken from the MESA Isochrones and Stellar Tracks (MIST) catalogue and assume solar metallicity. The tracks are computed with a mass spacing of 0.1,M$_\odot$. The data points are colour-coded according to seismic stellar mass. Squares denote stars with F-like, broad oscillation modes, circles correspond to the other stars, and markers with thick edges indicate stars exhibiting mixed modes (see Section 4.3 for details).

2. Observations and data preparation

2.1. Stellar sample description

Our sample comprises 32 MS and SG stars found to exhibit solar-like oscillations as part of Paper I. Among these, 10 stars are located within the PLATO LOPS2 field, while 24 are situated in the LOPN1 field. The global seismic parameters were derived using the `pySYD` pipeline (Chontos et al. 2022), as described in Paper I. Here, the frequency of maximum oscillation power, $\nu_{\rm max}$, corresponds to the frequency where the oscillation power spectrum reaches its maximum, while the large frequency separation, $\Delta\nu$, is defined as the average spacing between consecutive radial ($\ell = 0$) acoustic modes. These global seismic parameters scale with the stellar mass M, radius R, and effective temperature $T_{\rm eff}$ according to the asteroseismic scaling relations (Kjeldsen & Bedding 1995), such that

$$\frac{\nu_{\rm max}}{\nu_{\rm max,\odot}} \approx \left(\frac{M}{M_\odot}\right)\left(\frac{R}{R_\odot}\right)^{-2}\left(\frac{T_{\rm eff}}{T_{\rm eff,\odot}}\right)^{-1/2}, \quad (1)$$

and

$$\frac{\Delta\nu}{\Delta\nu_\odot} \approx \left(\frac{M}{M_\odot}\right)^{1/2}\left(\frac{R}{R_\odot}\right)^{-3/2}. \quad (2)$$

The values of $\Delta\nu$ and $\nu_{\rm max}$, along with the corresponding fundamental stellar parameters, are listed in Table 1. The seismic Hertzsprung–Russell (HR) diagram presented in Fig. 1 displays $\Delta\nu$ as a function of the effective temperature, with the colour scale indicating the seismic stellar mass. The masses were computed from Eqs. (1) and (2), adopting the solar reference values $\nu_{\rm max,\odot} = 3090\,\mu$Hz, $\Delta\nu_\odot = 135\,\mu$Hz, and $T_{\rm eff,\odot} = 5770$ K (Huber et al. 2011). For this purely illustrative representation in the HR diagram, no correction to $\Delta\nu$ was applied (e.g., White et al. 2011). The stars span a broad range of temperatures and seismic masses, illustrating the diversity of evolutionary states sampled from the main sequence to the sub-giant branch.

Table 1. List of the 34 TLS in the PLATO fields. Spectroscopic parameters are compiled from the literature (references given in the Ref. column), while global seismic parameters are taken from Paper I. The number of TESS observing sectors is reported separately for each cadence, and the notes indicate system multiplicity and some stellar properties.

Name	TIC	$T_{\rm eff}$ [K]	$\log g$	[Fe/H]	Ref.	$\nu_{\rm max}$ (I)	$\Delta\nu$ (I)	# 120s	# 20s	Note
Inside PLATO LOPS 2										
HR 3220	308844962	6483 ± 33	4.18 ± 0.05	−0.29 ± 0.03	(10)	1386.8 ± 27.0	71.6 ± 0.6	18	7	SB
HD 62644	123699670	5490 ± 50	3.816 ± 0.065	0.01 ± 0.044	(9)	708.4 ± 6.7	41.1 ± 0.3	8	4	BS
HD 50223	170225363	6437 ± 27	4.1 ± 0.07	−0.22 ± 0.04	(10)	1279.7 ± 66.0	69.0 ± 0.9	8	3	BS
ν^2 Col	32500750	6373 ± 70	3.94 ± 0.1	−0.11 ± 0.05	(10)	691.3 ± 43.5	38.9 ± 1.3	4	0	
171 Pup	149672905	5754 ± 22	4.11 ± 0.06	−0.85 ± 0.02	(10)	2107.7 ± 59.8	104.4 ± 0.9	5	3	SB
ζ Pic	219420836	6380 ± 38	4.0 ± 0.07	0.07 ± 0.04	(10)	853.0 ± 42.4	49.5 ± 0.4	7	2	
HD 36553	354552931	6002 ± 65	3.82 ± 0.06	0.35 ± 0.03	(10)	544.7 ± 16.1	33.7 ± 0.2	7	1	
HD 53705	130645536	5790 ± 15	4.33 ± 0.04	−0.22 ± 0.03	(13)	1989.9 ± 98.4	101.8 ± 0.7	8	5	
HD 46569	255630992	6313 ± 50	4.031 ± 0.059	0.04 ± 0.052	(9)	932.2 ± 20.5	49.7 ± 0.3	13	5	SB
HD 65907	372914091	5997 ± 16	4.52 ± 0.03	−0.31 ± 0.02	(10)	3006.9 ± 165.7	128.5 ± 1.2	19	13	
Inside PLATO LOPN 1										
χ Dra	341873045	6101 ± 25	4.29 ± 0.04	−0.64 ± 0.04	(10)	2314.7 ± 24.4	108.4 ± 0.1	38	16	SB
θ Dra	161825882	6196 ± 24	3.96 ± 0.17	0.2 ± 0.03	(10)	723.0 ± 15.8	40.2 ± 0.3	14	1	SB
θ Cyg	27014182	6914 ± 33	4.24 ± 0.01	−0.03 ± 0.03	(6)	1759.1 ± 67.1	82.8 ± 1.2	13	7	BS, EHC (5)
υ Cep	421444084	6161 ± 27	3.86 ± 0.08	0.12 ± 0.03	(10)	958.7 ± 22.3	53.6 ± 0.4	12	4	SB
ψ^1 Dra A	441804568	6410 ± 82	4.0 ± 0.05	0.01 ± 0.03	(10)	1232.4 ± 19.8	61.8 ± 0.3	39	18	SB
σ Dra	259237827	5298 ± 14	4.52 ± 0.02	−0.21 ± 0.01	(10)	4217.9 ± 122.6	182.2 ± 0.5	41	28	
ω Dra	233195546	6595 ± 28	4.19 ± 0.11	−0.03 ± 0.06	(3)	1999.5 ± 55.0	88.3 ± 2.0	39	19	SB
19 Dra	289622310	6298 ± 20	4.27 ± 0.07	−0.14 ± 0.02	(10)	2313.1 ± 493.9	104.8 ± 3.5	41	28	SB
36 Dra	233121747	6473 ± 38	4.09 ± 0.04	−0.29 ± 0.02	(10)	1312.0 ± 16.9	69.6 ± 0.2	36	14	
17 Cyg	58445695	6442 ± 63	4.17 ± 0.02	−0.07 ± 0.05	(2)	1484.4 ± 36.1	78.6 ± 1.5	5	3	
35 Dra	441813918	6191 ± 25	3.82 ± 0.05	−0.13 ± 0.04	(10)	705.3 ± 7.0	42.1 ± 0.1	40	13	
99 Her	22516402	5974 ± 23	4.2 ± 0.03	−0.55 ± 0.02	(10)	1950.7 ± 41.0	96.2 ± 0.6	5	4	SB
HD 136064	232563914	6144 ± 20	4.02 ± 0.04	−0.02 ± 0.02	(10)	1081.9 ± 23.8	59.1 ± 0.2	18	4	
HD 176051	20601206	5975 ± 20	4.54 ± 0.06	−0.1 ± 0.02	(10)	752.1 ± 11.3	43.5 ± 0.3	8	6	BS, 1 EH* (8)
26 Dra	219777482	5921 ± 33	4.44 ± 0.04	−0.04 ± 0.03	(10)	3059 ± 176.8	132.9 ± 0.9	40	27	SB
27 Cyg	41195655	5136 ± 27	3.66 ± 0.06	−0.02 ± 0.02	(10)	702.8 ± 44.4	40.6 ± 1.2	9	2	RS CVn
72 Her	9728611	5704 ± 13	4.33 ± 0.03	−0.39 ± 0.01	(10)	2241.4 ± 85.1	106.2 ± 1.0	5	3	
HD 175225	48194330	5297 ± 26	3.77 ± 0.08	0.14 ± 0.05	(10)	2902.2 ± 132.1	127.4 ± 1.7	23	5	
68 Dra	236871353	6270 ± 62	4.0 ± 0.13	−0.03 ± 0.04	(10)	716.2 ± 14.7	40.2 ± 0.6	20	5	
HD 184960	26884478	6287 ± 19	4.29 ± 0.06	−0.08 ± 0.03	(10)	1870.6 ± 73.9	91.9 ± 0.9	13	11	1 EH (2)
HD 191195	405902259	6730 ± 63	4.18 ± 0.02	−0.05 ± 0.05	(2)	1353.0 ± 146.7	69.2 ± 2.3	11	6	
HD 193664	403585118	5930 ± 18	4.48 ± 0.03	−0.1 ± 0.02	(11)	3174.6 ± 201.7	138.5 ± 2.8	26	17	
16 Cyg A	27533341	5791 ± 9	4.29 ± 0.02	0.08 ± 0.01	(10)	2236.5 ± 97.9	103.5 ± 1.1	12	10	BS
HD 152303	233503400	6573 ± 80	-	-	(3)	1689.5 ± 49.6	82.2 ± 1.5	34	14	

References. (1) Aguilera-Gómez et al. (2018); (2) **?**; (3) Casagrande et al. (2011); (4) Chontos et al. (2022); (5) Desort et al. (2009); (6) Koleva & Vazdekis (2012); (7) Lund et al. (2025); (8) Muterspaugh et al. (2010); (9) Perdelwitz et al. (2024); (10) Soubiran et al. (2022); (11) Soubiran et al. (2024);

Notes. Values of $\nu_{\rm max}$ and $\Delta\nu$ were computed with the `pySYD` pipeline in Paper I (Chontos et al. 2022; Lund et al. 2025). Abbreviations: RS CVn: RS Canum Venaticorum–type variable; BS: binary or multiple system; SB: spectroscopic binary; EH: confirmed exoplanet host (* indicates a confirmed planet in the system but not necessarily orbiting the target star); EHC: exoplanet host candidate. # 120s: number of sectors observed at 120-s cadence; # 20s: number of sectors observed at 20-s cadence.

2.2. Data

We analysed TESS observations up to and including Sector 88. TESS is a NASA mission led by the Massachusetts Institute of Technology (MIT) and launched on April 18, 2018, performing high-precision, time-series photometric observations as part of an all-sky survey (Ricker et al. 2014). TESS is designed to achieve a photometric precision of 50 parts per million (ppm) for stars with TESS magnitudes between 9 and 15. Using four identical cameras, it observes the sky sector by sector with a field of view of 24° × 96° per sector. Each sector is monitored for approximately 27 days, with multiple cadence options available.

In this paper, we use both the standard Pre-search Data Conditioning Sample Aperture Photometry (PDCSAP) light curves produced by the TESS Science Processing Operations Center (SPOC) and light curves extracted from target pixel files using custom apertures with the K2P^2 pipeline (Lund et al. 2015), following the procedure described in Paper I. The data include observations obtained at 120-s cadence and, where available from Sector 27 onward, 20-s cadence. In sectors providing both cadences, the 20-s data were additionally binned to a 120-s cadence to take advantage of their typically lower noise properties (Huber et al. 2022). All original TESS data were downloaded from the Mikulski Archive for Space Telescopes (MAST[1]).

For targets requiring improved photometric precision, particularly bright or saturated stars, the custom-aperture light curves provided a significant improvement over the PDCSAP products and, in some cases, enabled the detection of oscillations not apparent in the standard light curves. All light curves were corrected for long-term and instrumental trends using the *Kepler* Asteroseismic Science Operations Center (KASOC) filter (Handberg & Lund 2014). The power spectral density (PSD) was then computed from the filtered time series using a Lomb–Scargle periodogram (Lomb 1976; Scargle 1982) and normalised according to Parseval's theorem.

θ Cyg required special treatment because its PSD exhibits a clear series of harmonics, with a fundamental peak corresponding to a period of about 0.2815 days (or 6.7560 hours) close to what was previously reported by Guzik et al. (2016). Such a harmonic pattern is typically indicative of a non-sinusoidal periodic signal and may be associated with a transit or eclipse event in the light curve, either intrinsic to the target or arising from a contaminating companion within the TESS photometric aperture. Folding the light curve at this frequency reveals a distinct, regularly recurring flux dip. After removing the data points associated with this feature and recomputing the PSD, the harmonics linked to the binarity or transit signature disappear, enabling a reliable seismic analysis.

3. Mode extraction methods and strategy

The properties of the stellar oscillations were inferred through a detailed peak-bagging analysis carried out with three independent frameworks: `apollinaire` (Breton et al. 2022), FAMED (Corsaro et al. 2020), and `PBjam` (Nielsen et al. 2021, 2025). Each pipeline independently models the observed power spectral density to recover the frequencies, amplitudes, and linewidths of the oscillation modes. Below, we describe how each method was implemented and optimised.

3.1. `apollinaire`

The `apollinaire` module (Breton et al. 2022) was developed to extract seismic parameters directly in the Fourier domain using an ensemble-sampling Markov Chain Monte Carlo (MCMC) approach implemented with `emcee` (Foreman-Mackey et al. 2013). The analysis begins with the removal of the stellar background signal, which is modelled as the sum of one to three Harvey-like profiles (Harvey 1985), a Gaussian envelope centred on $\nu_{\max}$ to describe the p-mode power excess, and a constant white-noise component.

Initial estimates of the individual oscillation mode parameters were obtained from the global pattern fit for solar-like MS stars. The detailed procedure is discussed in Appendix A. For stars exhibiting more complex oscillation spectra, these initial estimates were instead obtained using the `iechelle`[2] pipeline, which allows the user to manually select preliminary frequency estimates from échelle diagrams. In this case, the initial mode identification followed the prescription of White et al. (2012), with the phase offset ε inferred from the estimated mode frequencies, while the large frequency separation $\Delta\nu$ was adopted from Paper I together with the effective temperature listed in Table 1. The parameter priors were then manually adjusted to maintain distinct frequency windows for neighbouring modes, thereby preventing overlap and improving the stability of the MCMC sampling.

These initial estimates were used as starting points for the simultaneous sampling of the joint posterior distribution. Each oscillation mode, characterised by its angular degree ℓ and radial order n, was modelled as a symmetric Lorentzian profile, with the central frequency $\nu_{n\ell}$ treated as a free parameter. The mode heights were parametrised according to

$$H_{\mathrm{n},\ell} = A_\ell \, H_{\mathrm{n},0} \text{ for } \ell = 0, 1\,, \tag{3}$$

$$H_{\mathrm{n},\ell} = A_\ell \, H_{\mathrm{n}-1,0} \text{ for } \ell = 2, 3\,, \tag{4}$$

where $A_0 = 1$ by definition, and the relative amplitudes A_ℓ for $\ell \neq 0$ were fitted. The linewidths $\Gamma_{\mathrm{n}\ell}$ were assumed to be common among groups of modes with degrees $\ell = (0, 1, 2, 3)$ and radial orders $(n, n, n+1, n+1)$, respectively. To ensure uniform priors across all sampled parameters, the MCMC was performed in terms of $\log \Gamma_{\mathrm{n},0}$, $\log H_{\mathrm{n},0}$, A_ℓ, and $\nu_{\mathrm{n},\ell}$. Convergence of the sampling and the absence of strong parameter degeneracies were assessed through visual inspection of the marginalised posterior distributions and two-dimensional corner plots.

3.2. FAMED

The peak-bagging analysis based on the adoption of the Diamonds code[3] (Corsaro & De Ridder 2014) relies on performing a preliminary step that fits the background signal of the stellar PSD. The background signal comprises granulation activity at two different scales, long-trend variation related to instrumental noise, potential magnetic activity and rotational effects, and the white noise. For this purpose, we have adopted the Background code extension of Diamonds[4]. Once the background fit is estimated, we adopt the peak-bagging pipeline FAMED (Corsaro et al. 2020) for an automated extraction and mode identification of the significant oscillation peaks that can be found in the power excess of the stellar PSD. The mode identification method used here is summarised in Sect. A.3.

---

[1] https://archive.stsci.edu

[2] Available at `https://gitlab.com/dinilbose/iechelle.git`

[3] `https://github.com/EnricoCorsaro/DIAMONDS`

[4] `https://github.com/EnricoCorsaro/Background`

3.3. `PBjam`

`PBjam`[5] (Nielsen et al. 2021, 2025) was also used to perform peak-bagging on this stellar sample, following the methodology described in Hookway et al. (2025). The analysis proceeds in two stages: an initial mode-identification step followed by detailed peak-bagging.

During mode identification, a background model consisting of three Harvey-like profiles (Harvey 1985) and a white-noise component is fitted to the power spectrum. This model is combined with a sum of Lorentzian profiles describing the radial and quadrupole ($\ell = 0, 2$) modes (Anderson et al. 1990), whose frequencies are estimated following the procedure described in Appendix A. In this framework, mode identification is formulated as a Bayesian inference problem in which asymptotic parameters and individual mode frequencies are inferred simultaneously from the power spectrum. The posterior distributions quantify both the most probable mode identification and the associated uncertainties, allowing ambiguous or noise-dominated peaks to be distinguished from genuine oscillation modes. Posterior sampling is performed with the `dynesty` nested sampling algorithm (Speagle 2020). Priors are informed by a large dataset of previously analysed stars and stellar models, enabling existing knowledge of oscillation patterns to guide the identification of mixed modes. The treatment of dipole ($\ell = 1$) modes depends on the evolutionary stage of the star. For stars without visible mixed modes, $\ell = 1$ modes are modelled as Lorentzian profiles, similarly to $\ell = 0$ and $\ell = 2$. For stars exhibiting mixed dipole modes, the asymptotic relation for $\ell = 1$ gravity modes is included, as described in Sect. A.2.

The parameters inferred during the identification stage are then used as priors for the detailed peak-bagging step, where the model constraints are relaxed. Frequency priors are defined as β distributions, i.e., continuous probability distributions bounded on a finite interval and parametrised by two positive shape parameters (α,β) that control their symmetry and concentration. These distributions were mapped onto an interval of width $\delta\nu_{02}/2$ centred on the initial estimate. Symmetric priors with $\alpha = \beta = 5$ are adopted, favouring the asymptotic frequency while allowing deviations within the prescribed range, for example due to acoustic glitches (Mazumdar et al. 2014). Normal priors are used for the logarithms of the mode widths and heights, centred on the identification-stage values with a standard deviation of 50 %.

Posterior distributions are sampled with the `emcee` MCMC algorithm. To assess the reliability of the inferred frequencies, the median absolute deviation of the posterior distributions is compared with the standard deviation of the corresponding β priors. This posterior-to-prior ratio quantifies the contribution of the data, and modes with ratios below 2/3 are considered validated and retained for further analysis.

4. Results and analysis

To characterise the oscillation spectra, we first applied the `apollinaire` pipeline to the four different light-curve datasets per star: 20-s cadence data calibrated using either the SPOC or K2P^2 procedures, and combined 20-s and 120-s cadence data processed with the same two calibrations. Owing to the low-frequency filtering applied to the light curves, a simplified background description was sufficient, combined with a cut at low frequency adapted for each star. Two Harvey-like components were required for 17 stars, while a single component adequately described the remaining 15, in all cases providing a reliable characterisation of the background across the p-mode frequency range. Background fitting converged for at least one dataset for every star in the sample. Individual oscillation modes were then fitted using the background-corrected power density spectra. Comparing the resulting mode frequencies across datasets enabled us to evaluate the impact of cadence and calibration choices, leading to the a posteriori selection of a reference dataset for each star based on the internal consistency and quality of the `apollinaire` results.

4.1. Choice of the reference dataset

To quantify the level of agreement between the different datasets, we evaluated, for each dataset i, the deviation of its measured mode frequencies from a consensus estimate defined by the remaining datasets. This analysis is restricted to stars for which at least three out of the four datasets yielded peak-bagging results. For a given mode (n, ℓ), this deviation is defined as

$$\Delta_{i,n\ell} = \nu_{i,n\ell} - \bar{\nu}_{j\neq i,n\ell} \,, \tag{5}$$

where $\nu_{i,n\ell}$ is the frequency measured in dataset i, and $\bar{\nu}_{j\neq i,n\ell}$ is the weighted mean of the frequencies obtained from all other datasets $j \neq i$. The significance of the deviation $\Delta_{i,n\ell}$ is quantified using a Z-score, which represents the number of standard deviations a data point is from the mean:

$$Z_{i,n\ell} = \frac{\Delta_{i,n\ell}}{\sigma_{\Delta_{i,n\ell}}} \,, \tag{6}$$

where the uncertainty $\sigma_{\Delta_{i,n\ell}}$ includes contributions from both datasets i and the weighted mean of the remaining datasets. Denoting by $\sigma_{i,n\ell}$ and $\sigma_{j,n\ell}$ the uncertainties associated with the frequency measurements $\nu_{i,n\ell}$ and $\nu_{j,n\ell}$, respectively, and assuming independent Gaussian errors, the variance of the deviation can be written as

$$\sigma^2_{\Delta_{i,n\ell}} = \sigma^2_{i,n\ell} + \left(\sum_{j\neq i} \frac{1}{\sigma^2_{j,n\ell}} \right)^{-1} . \tag{7}$$

This Z-score therefore measures how far the frequency reported by dataset i lies from the weighted mean of all other datasets. Values of $|Z| \lesssim 1$ indicate agreement within the quoted uncertainties, while larger values highlight tensions between datasets for a given mode. The different datasets for each star do not always cover exactly the same time span, which can introduce small variations in the measured mode frequencies. These differences arise because solar-like oscillations are stochastically excited (Goldreich & Keeley 1977; Samadi & Goupil 2001; Belkacem et al. 2008) and intrinsically damped (Belkacem et al. 2012), hence their amplitudes and phases fluctuate over time. In addition, magnetic activity can shift mode frequencies slightly on timescales comparable to the observation windows (e.g. García et al. 2010; Régulo et al. 2016; Santos et al. 2019). While our reference-dataset selection accounts for statistical consistency across datasets, these intrinsic temporal effects may contribute to the residual deviations captured by the Z-scores.

The reference dataset is selected by maximising the temporal coverage while minimising systematic deviations with respect to the other datasets. Specifically, we aim to maximise the number of observed sectors and minimise the median Z-score, med $|Z_{i,n\ell}|$, computed over all modes in dataset i. The selection procedure is as follows:

---

[5] https://github.com/PBjam-projects/PBjam

Table 2. Background parameters from the `apollinaire` fitting procedure.

Name	version	$n_{\mathcal{H}}$	low cut	$A_{\mathcal{H}_1}$	$\nu_{\mathrm{c},\mathcal{H}_1}$	$A_{\mathcal{H}_2}$	$\nu_{\mathrm{c},\mathcal{H}_2}$	$H_{\max}$	$\nu_{\max}$	W_{env}	P_{n}
HD 36553	20s & 120s (K2P^2)	2	80	12.81±0.79	203±15.63	4.4±0.77	602.72±33.94	8.08±0.57	573.42±6.2	116.25±12.71	3.77±0.02
θ Dra	20s & 120s (K2P^2)	1	200	14.37±2.48	157.7±16.82	-	-	3.69±0.14	616.66±14.37	334.53±14.94	1.04±0.01
ν^2 Col	120s (K2P^2)	1	80	20.65±1.9	167.05±12.66	-	-	3.69±0.35	670.01±14.92	207.43±26.67	3.4±0.02
HD 62644	20s & 120s (K2P^2)	2	120	21.24±2.61	165.55±9.22	4.77±0.23	637.36±14.37	10.03±0.49	704.17±2.64	84.65±4.32	1.84±0.01
68 Dra	20s & 120s (K2P^2)	2	80	12.18±0.35	224.04±7.33	2.34±0.26	750.72±33.91	4±0.24	711.83±7.26	157.44±13.89	4.42±0.01
35 Dra	20s (K2P^2)	2	80	6.87±0.25	247.13±9.85	1.51±0.27	811.48±43.61	4.16±0.2	712.86±7.49	202.06±9.76	0.99±0
27 Cyg	20s & 120s (K2P^2)	2	100	16.57±1.02	184.19±8.06	4.32±0.32	587.6±23.92	1.77±0.27	730.25±10.47	99.29±16.09	2.78±0.01
HD 175225	20s & 120s (K2P^2)	2	150	16.57±1.36	194.79±7.81	4.2±0.16	681.55±14.57	3.93±0.19	776.55±3.65	108.76±6.45	2.87±0.01
ζ Pic	20s & 120s (SPOC)	1	100	8.7±0.47	253.48±13.12	-	-	2.79±0.17	875.65±10.61	232.31±16.11	2.86±0.01
HD 46569	20s (K2P^2)	2	80	4.74±0.23	329.54±17.52	0.86±0.22	1115.27±112.38	2.84±0.21	929.85±10.82	204.93±17.81	1.7±0.01
υ Cep	20s & 120s (K2P^2)	1	100	3.72±0.14	267.62±10.3	-	-	0.81±0.04	1024.59±13.09	333.82±22.61	1.04±0
HD 136064	20s (K2P^2)	1	80	6.94±0.34	274.13±12.23	-	-	2.2±0.11	1079.18±10.76	279.65±15.37	1.13±0.01
ψ^1 Dra A	20s (K2P^2)	2	100	1.5±0.04	405.91±10.95	0.42±0.04	1370.37±42.39	0.51±0.03	1248.93±15.63	281.1±24.38	0.6±0
HD 191195	20s (K2P^2)	2	80	1.38±0.77	156.27±58.61	2±0.22	538.58±46.02	1.26±0.07	1330.31±63.18	701.97±89.25	2.2±0.01
HD 50223	20s & 120s (K2P^2)	1	100	3.21±0.13	417.61±19.6	-	-	1.08±0.09	1339.29±19.33	315.7±34.89	2.05±0.01
36 Dra	20s & 120s (K2P^2)	1	150	3.41±0.07	439.96±10.39	-	-	1.5±0.04	1354.15±6.61	348.77±10.2	1.84±0.01
HR 3220	20s & 120s (SPOC)	2	50	11.27±1.15	77.63±3.84	2.77±0.07	501.22±9.94	0.92±0.03	1368.51±19.23	529.94±29.16	1.58±0.01
HD 152303	20s (K2P^2)	2	55	5.06±0.49	102.7±6.56	1.54±0.08	545.14±29.12	0.63±0.04	1544.53±113.29	986.96±180.56	2.63±0.01
17 Cyg	20s (K2P^2)	1	50	2.75±0.12	423±21.11	-	-	0.78±0.07	1584.21±28.46	408.98±43.87	1.16±0.01
θ Cyg	20s (K2P^2)	2	80	3.38±0.28	119.57±5.1	1.66±0.03	651.46±9.12	0.71±0.01	1657.55±15.6	764.84±22.27	0.75±0
HD 184960	20s (SPOC)	2	150	1.21±0.06	600.87±33.95	0.3±0.06	2178.79±304.45	0.68±0.08	1857.74±34.34	392.68±63.82	2.05±0.02
ω Dra	20s (K2P^2)	1	150	1.04±0.03	576.89±19.65	-	-	0.27±0.02	1936.96±26.64	539.44±42.35	0.9±0
99 Her	20s (K2P^2)	2	120	1.44±0.07	483.11±20.74	0.29±0.03	2243.33±319.22	0.51±0.07	1998.75±30.43	306.28±53.06	1.1±0.02
HD 53705	20s & 120s (K2P^2)	2	100	0.99±0.11	501.02±41.67	0.36±0.11	1239.21±194.67	0.37±0.06	2037.73±41.69	303.96±54.09	1.75±0.01
171 Pup	20s (K2P^2)	2	100	1.09±0.11	519.8±54.62	0.28±0.12	1612.01±456.68	0.63±0.09	2133.05±33.66	316.5±59.86	1.37±0.02
16 Cyg A	20s (K2P^2)	1	150	1.34±0.06	485.2±24.23	-	-	0.28±0.03	2159.18±44.16	473.23±65.73	1.34±0.01
72 Her	20s (SPOC)	1	200	3.1±0.23	484.6±32.79	-	-	0.5±0.11	2186.25±40.77	242.2±48.81	1.53±0.01
χ Dra	20s (K2P^2)	2	80	0.65±0.02	598.57±14.38	0.16±0.01	1966.68±212.16	0.35±0.02	2336.97±10.83	437.2±28.17	0.36±0
19 Dra	20s (K2P^2)	1	100	0.99±0.02	615.67±15.08	-	-	0.14±0.01	2706.51±49.8	763.94±99.3	0.97±0
HD 176051	20s (K2P^2)	1	100	1.06±0.05	564.68±38.56	-	-	0.18±0.04	2834.23±173.05	749.66±387.7	1.37±0.02
HD 65907	20s (K2P^2)	2	80	0.61±0.04	564.2±40.72	0.25±0.04	1895.19±224.65	0.19±0.05	3055.34±84.01	412.51±146.14	1.71±0.01
HD 193664	20s (K2P^2)	2	80	0.53±0.17	686.15±234.43	0.25±0.18	1529.04±799.34	0.19±0.07	3062.17±338.21	1310.4±641.45	2.13±0.04
26 Dra	20s (K2P^2)	1	80	0.83±0.02	649.78±23.75	-	-	0.04±0.02	3272.71±251.63	899.35±405.33	1.18±0.01
σ Dra	20s (SPOC)	2	80	0.56±0.01	646.82±15.29	0.18±0.02	3058.52±113.3	0.09±0.02	4611.55±118.33	934.5±89.85	0.64±0.02

Notes. The table lists the amplitudes and central frequencies of the Harvey components, the Gaussian parameters of the p-mode envelope, and the noise level. Results correspond to the reference dataset indicated in the version column. The number of Harvey profiles ($n_{\mathcal{H}}$) and the low-frequency cut-off applied before fitting are also reported.

1. For each dataset i, compute med $|Z_{i,\mathrm{n}\ell}|$ and count the number of modes $N_i^{\min|Z|}$ for which dataset i minimises $|Z_{i,\mathrm{n}\ell}|$.
2. When the number of sectors observed in 120-s cadence exceeds twice that of the 20-s cadence, and fewer than 5 sectors of 20-s data are available, priority is given to datasets combining 20-s and 120-s cadences, provided their Z-score statistics are comparable. If med $|Z_{i,\mathrm{n}\ell}|$ instead favours a 20-s-only dataset, the power spectral density and échelle diagram are inspected to validate this choice, by assessing the signal-to-noise ratio and the visibility of the largest possible number of modes.
3. In all other cases, preference is given to the dataset with the smallest med $|Z_{i,\mathrm{n}\ell}|$ and the largest $N_i^{\min|Z|}$, with particular emphasis on preserving 20-s cadence data when available.

For the four stars (θ Dra, ψ^1 Dra A, 16 Cyg A, and HD 53705) for which peak-bagging results were obtained from only two datasets, a similar approach was adopted, combining visual inspection with maximisation of the temporal coverage. For seven additional stars, the mode parameters could be evaluated from only a single dataset, which was therefore adopted as the reference. The fitted background parameters for the selected reference dataset are listed in Table 2 for each star. Mode-parameter extraction could not be performed for ν^2 Col, HD 65907, and HD 152303 due to the very low visibility of the oscillation modes, yielding 29 stars with individual mode frequencies. Nevertheless, the background could still be constrained, and the corresponding parameters are also reported in Table 2: for the 120-s cadence data in the case of ν^2 Col for which no 20-s observations are available, and for the 20-s cadence data with more than ten observed sectors for the two remaining stars, using the K2P^2 calibration. Out of the 32 stars in the sample, the $\nu_{\max}$ values derived in this step differ by more than 2-σ from the Paper I values for only six stars (θ Dra, HD 175225, υ Cep, 36 Dra, 17 Cyg, and σ Dra), while the remaining stars are consistent with Paper I. Similarly, all $\Delta\nu$ values agree with Paper I, except for θ Dra and 19 Dra, which exceed the 2-σ difference.

4.2. Pipelines comparison: Peirce criterion

Independent frequency estimates for each mode (n, ℓ) were obtained from the reference dataset of each star by three different fitters and their preferred fitting pipelines (`apollinaire`, FAMED, and `PBjam`), yielding $N \leq 3$ measurements per mode. Before any comparison, outliers were identified and removed using Peirce's rejection criterion (Peirce 1852; Gould 1855), which is applicable when measurements are drawn from a common parent distribution with random, normally distributed errors. Although the number of measurements per mode is small, the criterion can still be applied because it is designed to identify even a single anomalous observation in a small dataset. In this framework, a data point is rejected if excluding it increases the likelihood of the residual distribution, while accounting for the probability of observing the given number of abnormal measurements. The formulation introduced by Gould (1855), which proceeds iteratively, is implemented in the Python package `pareidolia`[6]. For each mode, an initial mean frequency and its root-mean-square dispersion are first computed from the full sample. A rejection factor is then evaluated under the assumption of one questionable measurement, and values exceeding this threshold are removed. When multiple points are rejected, the rejection factor is updated accordingly, and the procedure is repeated until convergence is reached. This approach yields, for each mode, a statistically consistent subset of retained measurements. Similar applications of this method in asteroseismology have proven effective for harmonising frequency determinations across independent analyses (e.g. Metcalfe et al. 2010; Campante et al. 2011; Mathur et al. 2011; Appourchaux et al. 2012b).

Following convergence of the rejection process, the remaining frequencies were organised into three categories. The minimal list comprises modes for which all pipelines report a valid measurement after outlier removal (flag 1 in the frequency tables; one example is shown in Appendix C, with the full set available in machine-readable format). The maximal list includes modes supported by at least two pipelines (flag 2). Modes detected by only a single fitter are flagged separately (flag 3).

To identify a reference pipeline for each star, we evaluated the agreement between individual measurements and the mean frequency derived from the minimal list. For each fitter k, we computed the normalised root-mean-square deviation of its frequencies following the prescription of Appourchaux et al. (2012b):

$$\sigma_{\mathrm{normdev,k}} = \sqrt{\frac{1}{N_{\mathrm{k}}}\sum_{n,\ell}\frac{\left|\nu^k_{\mathrm{n},\ell} - \langle\nu_{\mathrm{n},\ell}\rangle\right|^2}{(\sigma^k_{\mathrm{n},\ell})^2}}\,, \qquad (8)$$

where $\nu^k_{\mathrm{n},\ell}$ and $\sigma^k_{\mathrm{n},\ell}$ denote the measured frequency value and its uncertainty, and N_{k} is the number of modes available for dataset k. Among the datasets providing valid measurements for at least half of the modes in the minimal list, the one exhibiting the smallest normalised deviation should be adopted as the reference for subsequent modelling.

If mode parameters were obtained by only two pipelines for a given star, the minimal list is formed from the modes fitted by both, and no reference set is adopted.

4.3. Sample analysis

This section presents the seismic parameters extracted from the reference datasets of 29 stars, enabling a detailed characterisation of their oscillation properties and evolutionary states. The number of fitted modes per star and per pipeline is listed in Table 3. The $\Delta\nu$ reported in the same table was derived from the $\ell = 0$ mode frequencies of the reference dataset through a weighted linear fit as a function of radial order. The fit was restricted to modes within $\pm 3\,\Delta\nu$ of $\nu_{\max}$ (Table 2). It accounts for the frequency uncertainties and the uncertainty on $\Delta\nu$ was estimated from the covariance matrix. For stars without a uniquely identified reference pipeline, the dataset containing the largest number of fitted modes was adopted as reference and marked with an asterisk in Table 3. For two stars (θ Dra and HR 3220), the three pipelines did not converge on a consistent mode identification. This is partly due to their location in a temperature regime where the asymptotic phase term, ε, is highly sensitive to small changes in effective temperature (e.g. White et al. 2012). This is discussed further in the next section. For these stars, the échelle diagrams in Appendix B show the detected modes with their respective identifications, and the reference set was taken to be the dataset with the largest number of modes, namely FAMED in both cases.

From a visual inspection of the échelle diagrams for the full sample, 13 stars were classified as F-like (Table 3). These stars exhibit broad, overlapping ridges caused by the combination of large linewidths and small inter-degree frequency separations,

---

[6] available at https://gitlab.com/evapanetier/pareidolia.git

Table 3. Number of fitted modes per pipeline for each of the 29 stars, together with the number of modes retained in the minimal list. We additionally report the large frequency separations, $\Delta\nu$, measured by the reference pipeline. The stars are ordered by $\nu_{\max}$ (Table 2).

Name	Number of fitted modes				Reference	Note	$\Delta\nu$ (μHz)
	`apollinaire`	FAMED	`PBjam`	Minimal list			
HD 36553	32	25	15	15	`apollinaire`	F-like, mixed	33.54 ± 0.06
θ Dra	34	35	15	≠ mode id.	FAMED*	Solar-like, mixed	39.38 ± 0.10
HD 62644	37	23	24	22	`apollinaire`	Solar-like, mixed	41.12 ± 0.04
68 Dra	38	35	10	8	`apollinaire`	F-like, mixed	39.66 ± 0.11
35 Dra	39	36	38	31	`apollinaire`	F-like, mixed	41.87 ± 0.06
27 Cyg	27	26	17	13	`apollinaire`	Solar-like, mixed	39.85 ± 0.05
HD 175225	40	35	26	24	`apollinaire`	Solar-like, mixed	43.51 ± 0.03
ζ Pic	45	38	17	16	`apollinaire`	Solar-like, mixed	49.35 ± 0.13
HD 46569	35	27	15	13	`apollinaire`	F-like	49.92 ± 0.11
υ Cep	29	52	17	15	`apollinaire`	Solar-like, mixed	53.79 ± 0.13
HD 136064	30	32	16	16	`apollinaire`	F-like	59.38 ± 0.09
ψ^1 Dra A	30	35	28	20	`apollinaire`	F-like	61.87 ± 0.21
HD 191195	47	–	–	–	`apollinaire`*	F-like	71.24 ± 0.21
HD 50223	47	–	11	10	`apollinaire`*	F-like	69.04 ± 0.15
36 Dra	39	50	17	17	`PBjam`	F-like	69.99 ± 0.23
HR 3220	24	38	17	≠ mode id.	FAMED*	F-like	71.17 ± 0.02
17 Cyg	39	29	13	13	`apollinaire`	F-like	78.99 ± 0.14
θ Cyg	29	–	–	–	`apollinaire`*	F-like	83.80 ± 0.11
HD 184960	31	20	17	13	`apollinaire`	Solar-like, low SNR	91.73 ± 0.12
ω Dra	24	–	21	7	`apollinaire`*	F-like, low SNR	89.17 ± 0.41
99 Her	26	19	26	17	`apollinaire`	Solar-like	96.04 ± 0.16
HD 53705	27	10	16	10	`apollinaire`	Solar-like	101.55 ± 0.13
16 Cyg A	24	16	16	10	`apollinaire`	Solar-like	103.27 ± 0.21
72 Her	47	11	15	9	`apollinaire`	Solar-like	106.58 ± 0.28
19 Dra	24	–	23	23	`apollinaire`*	Solar-like, low SNR	115.48 ± 0.11
HD 176051	30	–	–	–	`apollinaire`*	Solar-like, low SNR	126.55 ± 0.20
HD 193664	32	3	17	3	`PBjam`	Solar-like, low SNR	137.18 ± 0.11
26 Dra	14	–	6	6	`apollinaire`*	Solar-like, low SNR	131.26 ± 0.13
σ Dra	24	–	22	22	`apollinaire`*	Solar-like, low SNR	182.07 ± 0.10

Notes. When available, the minimal list comprises modes fitted by all three pipelines and classified as non-outliers according to the Peirce criterion. If only two pipelines successfully analysed a star, it includes the modes common to those two. For three stars, no consistent mode identification was achieved across pipelines, and a minimal list was therefore not defined. The reference pipeline selected following the procedure described in Sect. 4.2 is also indicated. If no reference set could be determined, the dataset with the largest number of extracted modes was adopted as reference and marked with an asterisk.

and they occupy the upper region of the HR diagram (Fig. 1), corresponding to higher effective temperatures and lower large frequency separations. This behaviour reflects the shorter mode lifetimes expected in hotter stars with shallower convective envelopes. In contrast, nine stars show evidence of mixed modes detected by at least one pipeline and are highlighted in Fig. 1. These mixed modes appear as disrupted or distorted ridges in the échelle diagrams and arise from the coupling of p- and g-mode cavities as stars evolve off the main sequence (e.g. Benomar et al. 2013). Among these stars, three are classified as F-like and five as solar-like, spanning a range of evolutionary stages. Some exhibit a fully disrupted $\ell = 1$ ridge (HD 62644, 27 Cyg, and HD 175225), others retain a recognisable ridge while showing several mixed modes outside the ridge (θ Dra, 68 Dra, and υ Cep), and the remaining stars likely display only a single $\ell = 1$ mode outside the ridge (HD 36553, 35 Dra, and 36 Dra).

The identification of mixed modes differs significantly between pipelines, reflecting both methodological choices described in Appendix A, and the intrinsic complexity of mixed-mode spectra. Using `PBjam`, a dedicated mixed-mode fitting was performed for seven stars, while FAMED also detected out-of-the-ridge modes in seven stars, which do not entirely overlap with the `PBjam` sample. Since `apollinaire` does not automatically detect mixed modes, unlike the other two pipelines, we applied the procedure described in Sect. A.2 to model mixed-mode frequencies and compare them with the observations, allowing genuine modes to be distinguished from noise. The key results regarding mixed-mode detection are listed below:

- Both `PBjam` and FAMED identify mixed modes in θ Dra, HD 62644, 68 Dra, 27 Cyg, and HD 175225. HD 36553 and ζ Pic are detected only with `PBjam`, while 35 Dra and υ Cep are identified solely by FAMED.
- The procedure used for `apollinaire` results successfully identified $\ell = 1$ mixed-mode patterns in HD 62644 and HD 175225. For the remaining seven stars, the method did not converge, either because an insufficient number of mixed modes was available to constrain the fit or, in the case of 27 Cyg and ζ Pic, despite the presence of numerous detected modes.
- For several targets, discrepancies between pipelines mainly concern the number of detected mixed modes. In θ Dra and υ Cep, FAMED identified five and twelve $\ell = 1$ modes, respectively, located outside the main ridges and not recovered

by the other pipelines. By contrast, `apollinaire` identified additional mixed modes not recovered by FAMED or `PBjam`, reporting seven such modes in HD 62644 that are all consistent with the mixed-mode identification procedure, and a further seven $\ell = 1$ modes in ζ Pic that do not show the same consistency with this procedure.

- In other cases, discrepancies reflect marginal detections rather than fundamentally different interpretations. For 68 Dra, mode detection varies across pipelines, with several modes detected by only one method. Similarly, for 27 Cyg and HD 175225, three (resp. two) mixed modes were identified by `PBjam`, whereas six (resp. four) additional modes were detected by the other two pipelines but not recovered by `PBjam`.
- For 35 Dra, a single mode located outside the $\ell = 2$ ridge was classified as $\ell = 1$ by FAMED and as $\ell = 2$ by `apollinaire`. Given its systematic offset from the $\ell = 2$ ridge and its similarity to mixed modes observed in comparable stars (e.g. Appourchaux 2020), this mode is most likely of mixed character. Residual power in the échelle diagram further suggests that additional mixed modes may remain undetected.

The diversity in mixed-mode morphology reflects differences in core structure and evolutionary state across the sample. Thus, stars exhibiting a larger number of detectable mixed modes tend to be more evolved.

The p-mode envelope of at least eight stars in our sample (HD 36553, θ Dra, ζ Pic, υ Cep, HD 136064, HD 50223, 17 Cyg, and θ Cyg) departs from the classical Gaussian-like shape, instead exhibiting a double-humped or plateau-like structure, as seen in their respective PSD in Appendix B. Similar broad, non-Gaussian envelopes have long been observed in the bright F5 sub-giant Procyon, which has become a benchmark case for such atypical solar-like oscillation profiles (e.g. Bedding et al. 2005). Comparable features have also been reported in several stars observed by CoRoT and *Kepler* (e.g., Mathur et al. 2010; García & Ballot 2019), and were specifically noted by Guzik et al. (2016) for θ Cyg. Stars displaying this type of envelope tend to be hotter and, in some cases, slightly evolved subgiants. We suggest that compiling a dedicated sample of such targets could provide valuable insight into the physical origin of these non-standard envelope morphologies.

Two stars in our sample were also observed by *Kepler*: θ Cyg (Guzik et al. 2016) and 16 Cyg A (Metcalfe et al. 2012; Davies et al. 2015; Lund et al. 2017). These literature frequencies are shown in the échelle diagrams of the stars (Figs. B.18 and B.23). For 16 Cyg A, all three studies report very similar values, so only the most recent set (Lund et al. 2017) is displayed. Twenty-four modes are common between our measurements and the literature for this latter star, all agreeing within 2,σ. In the case of θ Cyg, 26 modes were extracted from both *Kepler* and TESS observations. Of these, 12 modes from our analysis are consistent within 2 σ of the Guzik et al. (2016) values, while 9 modes differ by more than 3 σ. These discrepancies are primarily associated with modes at the edges of the p-mode envelope, where the oscillation amplitudes are lower, and the signal-to-noise ratio is reduced. In addition, as an F-type star, θ Cyg exhibits intrinsically broad oscillation modes, which overlap in the power spectrum and are more challenging to fit accurately. The combination of low amplitude and broad mode width likely accounts for the observed deviations from the Guzik et al. (2016) measurements. Similarly, σ Dra was also analysed by Hon et al. (2024) using both TESS photometry (sectors 41–60) and radial velocities from the Keck Planet Finder (KPF). Their extracted frequencies are shown alongside ours in Fig. B.29. Comparing the two TESS-based frequency sets, we identify two additional low-frequency modes, while they reported one additional mode at a higher frequency. We also detect quadrupolar modes that were not reported in their analysis. Aside from these differences, all commonly extracted frequencies agree within less than 1 σ.

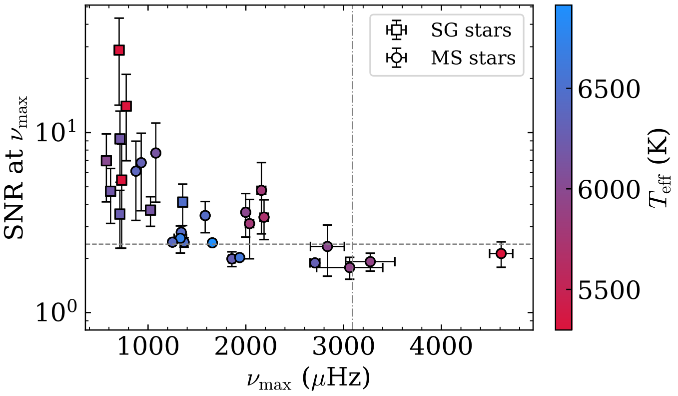

Fig. 2. Signal-to-noise ratio of the radial mode ($\ell = 0$) closest to $\nu_{\max}$, plotted as a function of $\nu_{\max}$ for each star. Markers are coloured according to the effective temperature of the stars listed in Table 1, and indicated by the colour bar. SG stars are shown as squares, while MS stars are circles. The low SNR threshold of 2.4 is indicated by a dashed horizontal line, and the solar value $\nu_{\max,\odot} = 3090\,\mu$Hz is marked by a dot-dashed vertical line.

The signal-to-noise ratio (SNR) of the radial mode closest to $\nu_{\max}$ was computed for each star using the `apollinaire` results and is shown as a function of $\nu_{\max}$ in Fig. 2. Uncertainties were estimated by propagating the errors in both the mode height (mean of lower and upper bounds) and the background parameters. As expected, stars with lower $\nu_{\max}$ tend to exhibit higher SNR, even though their apparent magnitudes are relatively similar ($V \in [3.55, 5.99]$, Paper I), confirming that the SNR trend is primarily driven by $\nu_{\max}$ rather than brightness differences. Seven stars have SNR values below 2.4 (Table 3), corresponding to cases where the mode ridges become increasingly difficult to discern in the échelle diagrams. For these stars, we added an additional panel in the échelle diagrams (Appendix B) showing the collapsed échelle (e.g. Bedding et al. 2005), which highlights the presence of mode ridges despite the low SNR. Stars in the solar $\nu_{\max}$ regime systematically exhibit low SNR in TESS observations. This limited SNR restricts our ability to constrain mode widths and therefore damping properties, which are key diagnostics of near-surface convection. These targets are therefore prime candidates for PLATO, whose higher photometric precision and longer time series will enable a more robust seismic characterisation. This aligns with PLATO's core objective of precisely determining stellar masses, radii, and ages for solar-like stars, thereby improving stellar model calibration and the characterisation of their planetary systems. For some of these stars (i.e. 19 Dra, HD 176051, 26 Dra, and σ Dra), the mode widths are not well constrained, as the base of the mode peaks is buried within the noise. Nevertheless, the extracted frequencies remain consistent with the peaks seen in the summed échelle power. Notably, despite its low SNR and high $\nu_{\max}$, close to the Nyquist frequency of the instrument at this cadence, mode frequencies were successfully extracted for σ Dra. This star therefore represents one of the coolest MS stars observed with TESS for which individual mode parameters have been robustly extracted and modelled (Hon et al. 2024).

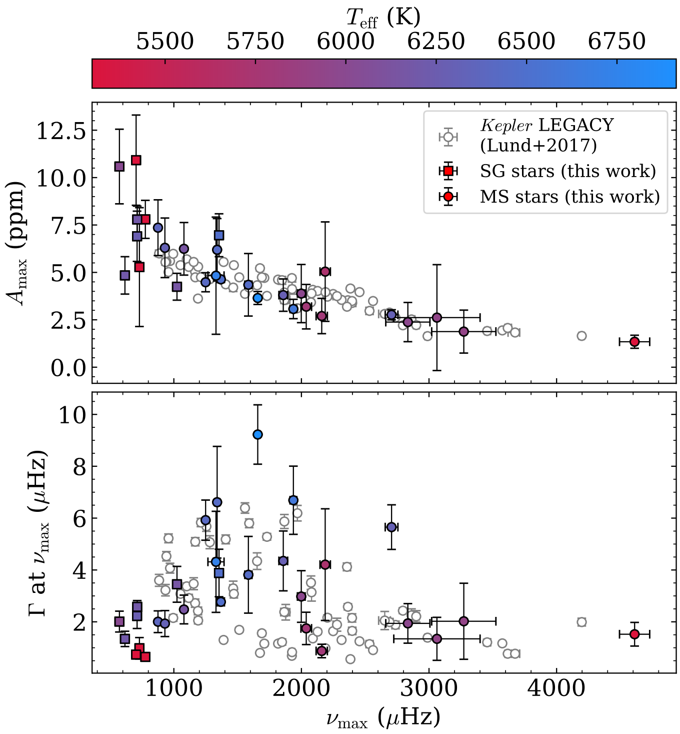

Fig. 3. Amplitude (top) and linewidth (bottom) of the radial mode closest to $\nu_{\rm max}$, plotted as a function of $\nu_{\rm max}$ for each star. Markers follow the same legend as in Fig. 2. For reference, stars from the *Kepler* LEGACY sample (Lund et al. 2017) are shown as grey markers in the background of the bottom two panels.

5. Discussion and comparisons with other studies

To place these results in a broader context, we further compare the seismic properties of our sample with stars from the *Kepler* LEGACY catalogue, a benchmark sample of 66 solar-like stars observed by *Kepler* with exceptionally high signal-to-noise data, providing some of the most precise seismic constraints currently available for stellar modelling. In this section, we consider only the reference dataset selected for each star, or, if none is defined, the dataset containing the largest number of fitted modes.

The amplitude and linewidth of the radial mode closest to $\nu_{\rm max}$ are shown as a function of $\nu_{\rm max}$ (values from Table 2) in Fig. 3. As previously observed for the *Kepler* LEGACY sample, the mode amplitude decreases with increasing $\nu_{\rm max}$. For main-sequence stars, it also decreases with decreasing effective temperature. Stars exhibiting mixed modes occupy the upper-left region of the amplitude panel and are associated with relatively small linewidths in the bottom panel, consistent with their more evolved nature and longer mode lifetimes. The linewidths display an overall bell-shaped dependence on $\nu_{\rm max}$: they are small at low $\nu_{\rm max}$, increase and become more dispersed at intermediate $\nu_{\rm max}$, and decrease again at higher $\nu_{\rm max}$. This behaviour reflects the known dependence of mode damping on stellar structure and effective temperature (Belkacem et al. 2012; Houdek et al. 2019). As discussed in the previous section, most stars with low SNR have poorly constrained linewidths, which likely explains the unusually large widths measured for the two stars near 1650 and 2700 μHz (θ Cyg and 19 Dra). Excluding these cases, all stars in our sample are consistent with the distribution defined by the LEGACY sample in terms of both $A_{\rm max}$ and Γ at $\nu_{\rm max}$, although our uncertainties are generally larger.

For each star, we computed the average small frequency separations, $\delta\nu$, and ε, following the procedure described in Lund et al. (2017). This was done by fitting the observed mode frequencies with

$$\nu_{n,\ell} \simeq \left(n + \frac{\ell}{2} + \varepsilon\right)\Delta\nu_0 - \delta\nu_{0,\ell} - \frac{{\rm d}\delta\nu_{0,\ell}}{{\rm d}n}\left(n - n_{\nu_{{\rm max},\ell}}\right) + \frac{{\rm d}\Delta\nu/{\rm d}n}{2}\left(n - n_{\nu_{{\rm max},\ell}}\right)^2, \quad (9)$$

where $\Delta\nu_0$ is the large frequency separation evaluated at $\nu_{\rm max}$, and $n_{\nu_{\rm max}}$ is the (generally non-integer) radial order corresponding to $\nu_{\rm max}$. The small separations $\delta\nu_{0,1}$ and $\delta\nu_{0,2}$ were optimised independently. In practice, we implemented this functional form through a parametric model in which $\Delta\nu_0$, ε, ${\rm d}\Delta\nu/{\rm d}n$, and $n_{\nu_{\rm max}}$ were treated as global parameters, while $\delta\nu_{0,\ell}$ and ${\rm d}\delta\nu_{0,\ell}/{\rm d}n$ were fitted separately for $\ell = 1$ and $\ell = 2$. Radial modes therefore constrain only the global parameters and the curvature term, while the dipole and quadrupole modes additionally constrain their respective small separations and gradients. The fit was performed by minimising the residuals between observed and modelled frequencies, weighted by the individual frequency uncertainties. We first obtained a maximum-likelihood solution using a least-squares minimisation (with `lmfit`, Newville et al. 2025), and subsequently explored the joint posterior distribution of the parameters using an MCMC approach. A Gaussian prior on $\nu_{\rm max}$ was included by requiring the modelled radial-mode frequency at $n_{\nu_{\rm max}}$ to reproduce the observed $\nu_{\rm max}$ (from Table 2) within its uncertainty. Final parameter estimates and uncertainties were derived from the marginalised posterior distributions and are listed in Table 4.

For three stars, only the global parameters $\Delta\nu_0$, ε, and ${\rm d}\Delta\nu/{\rm d}n$ were determined: HD 184960, where the fit did not converge toward physically meaningful values of the small frequency separations and the two stars for which no consensus on mode identification was reached (θ Dra and HR 3220). For these two latter stars, two estimates of ε were obtained. The value listed in Table 4 corresponds to the pipeline that extracted the largest number of modes (FAMED in both cases), while a second estimate was derived using `PBjam`, which adopted an alternative mode identification. These values are shown in Fig. 4, together with measurements from the LEGACY sample and the stars analysed by White et al. (2012), who provided ε and $\Delta\nu$ for 163 *Kepler* targets. The two stars (θ Dra and HR 3220, represented with yellow and blue diamonds) fall within the range defined by these reference samples, consistent with the rest of our targets. However, they are located close to the edges of the expected ε–$T_{\rm eff}$ relation, such that a modest shift in effective temperature could potentially change the preferred mode identification.

For the three stars showing numerous mixed modes (HD 62644, 27 Cyg, and HD 175225), for which a simple asymptotic description is inadequate, only $\delta\nu_{0,2}$ was estimated together with the global parameters. We emphasise that in other stars where mixed modes were detected, $\delta\nu_{0,1}$ and its variation in order n were still measured because a clear ridge associated with the underlying *p*-mode pattern was identified in their échelle diagram. In those cases, the presence of mixed modes did not prevent the extraction of reliable frequency separations. $\Delta\nu$ and ε are strongly correlated, so even a small variation in the inferred $\Delta\nu$ can significantly affect ε and, consequently, the angular-degree assignment of the ridges in the échelle diagram. When broad linewidths and, in some cases, mixed modes further complicate the pattern, this may result in substantial differences in mode

Table 4. Values from the fit of Eq. (9) to the mode frequencies.

Name	$\Delta\nu_0$ (μHz)	ε	d $\Delta\nu$/dn (μHz)	$\delta\nu_{0,1}$ (μHz)	d $\delta\nu_{0,1}$/dn (μHz)	$\delta\nu_{0,2}$ (μHz)	d $\delta\nu_{0,2}$/dn (μHz)
HD 36553	33.78 ±0.05	1.13 ±0.03	0.149 ±0.027	2.245 ±0.139	−0.081 ±0.062	2.415 ±0.266	−0.193 ±0.166
θ Dra	40.26 ±0.07	1.43 ±0.03	0.027 ±0.015	–	–	–	–
HD 62644	41.12 ±0.03	1.41 ±0.01	0.082 ±0.033	–	–	3.857 ±0.094	0.158 ±0.068
68 Dra	40.19 ±0.04	0.91 ±0.02	0.104 ±0.020	1.927 ±0.206	0.303 ±0.066	3.992 ±0.285	−0.128 ±0.093
35 Dra	41.95 ±0.06	1.21 ±0.02	0.278 ±0.009	3.306 ±0.103	−0.141 ±0.043	3.005 ±0.188	−0.534 ±0.067
27 Cyg	39.92 ±0.08	1.32 ±0.04	0.200 ±0.041	–	–	3.385 ±0.254	−0.150 ±0.112
HD 175225	43.60 ±0.03	1.33 ±0.01	0.241 ±0.011	–	–	3.681 ±0.069	−0.199 ±0.024
ζ Pic	49.71 ±0.05	0.99 ±0.02	0.083 ±0.022	2.617 ±0.243	0.359 ±0.060	3.952 ±0.330	0.445 ±0.102
HD 46569	49.77 ±0.09	1.08 ±0.03	0.352 ±0.028	2.324 ±0.198	−0.216 ±0.072	1.596 ±0.358	−0.322 ±0.121
υ Cep	53.83 ±0.13	0.99 ±0.05	0.462 ±0.028	2.952 ±0.210	−0.140 ±0.061	4.290 ±0.835	−0.332 ±0.171
HD 136064	59.49 ±0.09	1.15 ±0.03	0.305 ±0.032	3.535 ±0.237	0.234 ±0.093	4.431 ±0.286	−0.360 ±0.137
ψ^1 Dra A	61.92 ±0.09	0.86 ±0.03	0.166 ±0.020	0.887 ±0.365	−0.089 ±0.090	–	–
HD 191195	68.11 ±0.29	0.53 ±0.06	0.373 ±0.019	−1.549 ±0.789	0.005 ±0.102	3.143 ±0.874	−0.315 ±0.139
ξ Pup	68.54 ±0.10	1.05 ±0.03	0.325 ±0.015	0.666 ±0.222	−0.167 ±0.054	2.169 ±0.393	−0.373 ±0.075
36 Dra	69.99 ±0.14	1.00 ±0.04	0.232 ±0.076	4.101 ±0.281	0.180 ±0.160	5.593 ±0.627	−0.650 ±0.402
HR 3220	71.49 ±0.08	1.10 ±0.02	0.312 ±0.002	–	–	–	
17 Cyg	78.08 ±0.13	1.39 ±0.03	0.270 ±0.026	2.566 ±0.420	−0.578 ±0.098	3.634 ±0.402	−0.105 ±0.115
θ Cyg	82.98 ±0.01	1.00 ±0.00	0.397 ±0.020	0.514 ±0.218	−0.270 ±0.060	5.959 ±0.508	−0.488 ±0.098
HD 184960	91.84 ±0.21	1.21 ±0.05	0.433 ±0.106	–	–	–	–
ω Dra	88.62 ±0.11	0.94 ±0.03	−0.094 ±0.057	2.825 ±0.440	−0.359 ±0.131	8.151 ±1.166	0.339 ±0.431
99 Her	96.14 ±0.14	1.32 ±0.03	0.265 ±0.042	4.551 ±0.370	−0.538 ±0.115	4.643 ±0.771	−0.736 ±0.274
HD 53705	101.38 ±0.13	1.53 ±0.03	0.210 ±0.051	4.390 ±0.379	−0.913 ±0.111	4.688 ±0.406	−0.920 ±0.213
16 Cyg A	103.20 ±0.22	1.46 ±0.04	0.291 ±0.088	3.952 ±0.382	−0.097 ±0.250	6.588 ±0.838	−0.347 ±0.353
72 Her	105.95 ±0.13	1.52 ±0.02	0.314 ±0.016	2.736 ±0.316	−0.146 ±0.071	3.778 ±0.546	−0.467 ±0.114
19 Dra	115.09 ±0.09	1.19 ±0.02	0.169 ±0.036	4.521 ±0.261	0.259 ±0.081	12.407 ±0.414	−0.186 ±0.336
HD 176051	126.95 ±0.55	1.36 ±0.10	0.377 ±0.021	4.087 ±0.410	−0.055 ±0.115	8.753 ±0.745	−0.160 ±0.322
HD 193664	137.18 ±0.28	1.51 ±0.05	0.109 ±0.090	3.013 ±1.260	−0.593 ±0.148	8.975 ±2.161	−1.070 ±0.519
26 Dra	131.06 ±1.07	1.56 ±0.20	−0.725 ±0.108	3.914 ±0.813	0.071 ±0.260	–	–
σ Dra	182.49 ±0.17	1.50 ±0.02	0.223 ±0.024	4.006 ±0.247	−0.278 ±0.054	11.026 ±1.550	0.123 ±0.444

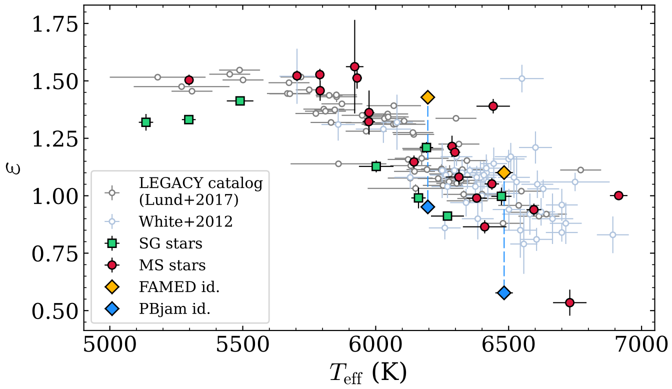

Fig. 4. ε as a function of effective temperature. SG stars are shown as green squares, and MS stars as red circles. The two stars for which the fitters did not reach agreement on the mode identification are indicated by diamonds, with FAMED identification in yellow, and `PBjam`'s one in blue, both symbols belonging to the same star being linked with a dashed blue line. For comparison, stars from the LEGACY catalogue are plotted in grey, while those from Table 1 of White et al. (2012) are shown in light blue. Error bars are shown where visible and are otherwise smaller than the marker size.

identification between pipelines. This underscores the strong interplay between effective temperature, global stellar structure, and mode pattern geometry in this regime.

The resulting small frequency separations, $\delta\nu_{0,1}$ and $\delta\nu_{0,2}$, and their ratio are shown in Fig. 5. The variations of $\delta\nu_{0,1}$ and $\delta\nu_{0,2}$ with radial order n (panels b and d) are larger than those reported in the LEGACY catalogue. However, as these variations are mostly zero or negative, they remain compatible with decreasing functions of frequency, in line with what was noted by Lund et al. (2017). We note a systematic negative offset in $d\delta\nu_{0,2}/dn$ between our sample and the LEGACY stars. This may be due to the shorter observation baseline and lower SNR of TESS compared with *Kepler*, which disproportionately affects the lower-amplitude $\ell = 2$ modes and increases the uncertainty in the derived slope. As noted by Lund et al. (2017), most stars deviate from the asymptotic regime. Only five stars in our sample (HD 50223, ω Dra, 19 Dra, HD 193664, and σ Dra) are compatible with the asymptotic ratio $\delta\nu_{0,2}/\delta\nu_{0,1} = 3$. Two stars, HD 191195 and θ Cyg, depart strongly from the asymptotic regime and are inconsistent with the distribution defined by the LEGACY sample, suggesting structural differences not captured by the asymptotic approximation. A revised interpretation of the small frequency separations, extending from the main sequence to more evolved stages, has recently been proposed, in which $\delta\nu_{0,2}$ is found to scale primarily with global seismic parameters rather than directly tracing the internal sound-speed gradient (Ong et al. 2025). Finally, ω Dra and 26 Dra lie below zero in panel (f), which shows d$\Delta\nu$/dn as a function of $\Delta\nu$, while all other stars cluster around ~0.25, consistent with Lund et al. (2017). These two stars, therefore, appear to exhibit a negative gradient of the large frequency separation with frequency, potentially indicating structural curvature effects. However, this result

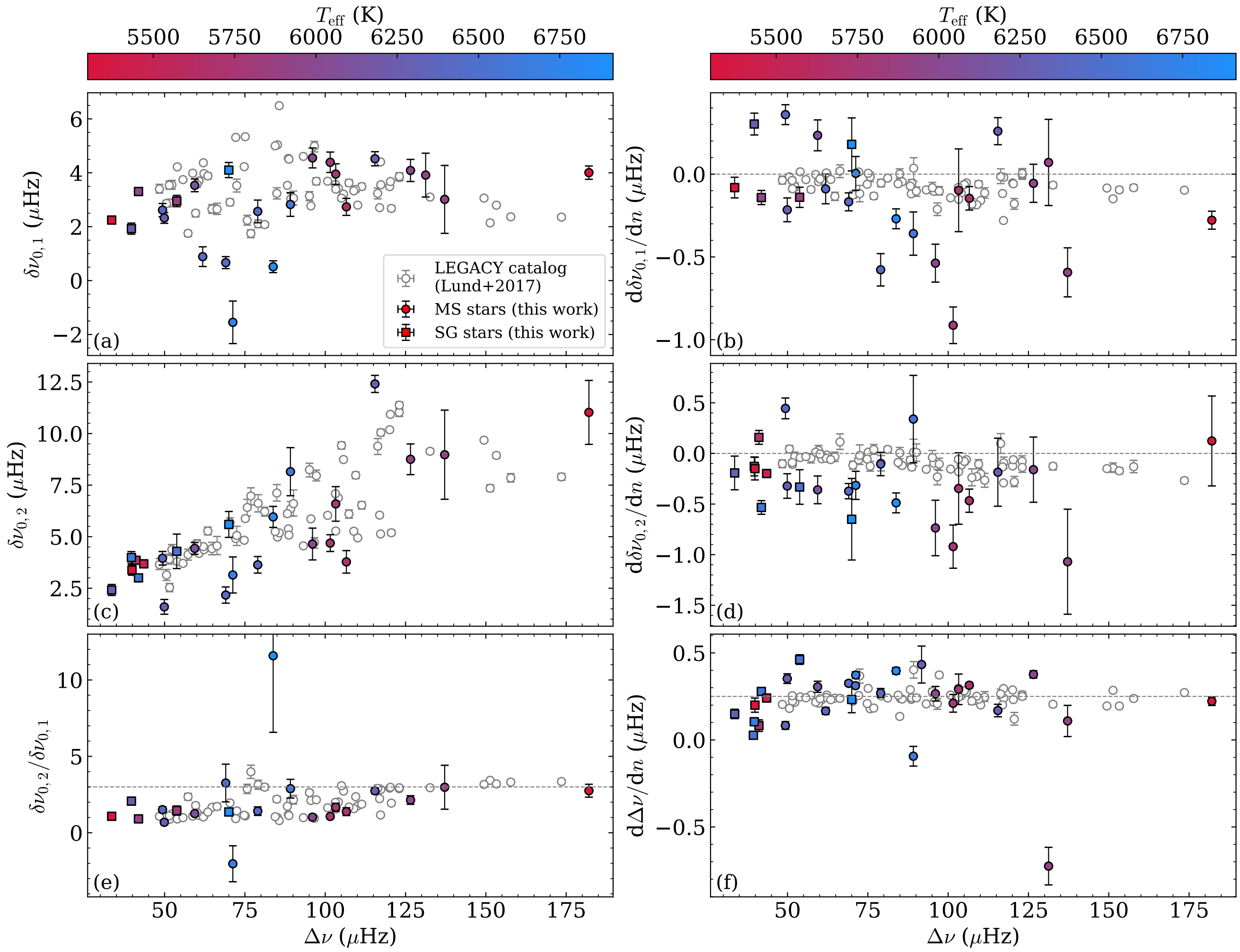

Fig. 5. The small frequency separations, $\delta\nu_{0,1}$ (panel a) and $\delta\nu_{0,2}$ (panel c), along with their variation with radial order n (panels b and d), and their ratio $\delta\nu_{0,1}/\delta\nu_{0,2}$ (panel e), are plotted as a function of $\Delta\nu$ (from Table 3) for each star. Panel (f) shows the variation of $\Delta\nu$ with n as a function of $\Delta\nu$, with the dashed line indicating the nearly constant value of $0.25\,\mu$Hz around which most stars appear to lie, as discussed in Lund et al. (2017). Markers are coloured according to the effective temperature of the stars listed in Table 1, and indicated by the colour bar. SG stars are shown as squares, while MS stars are circles. For reference, stars from the LEGACY sample (Lund et al. 2017) are shown as grey markers in the background. The dashed line in panel (e) indicates the expected value of 3 from the asymptotic relation in Eq. (A.1), while those in panels (b) and (d) show the zero value.

should be treated with caution, as both stars have relatively low SNR (Table 3), which may bias the inferred structure.

6. Conclusion

We present a detailed seismic analysis of 29 solar-like stars from a sample of 32 bright TESS targets that will be located in the PLATO LOP fields as identified in Paper I, focusing on the extraction of individual oscillation mode parameters. These stars are among the brightest solar-like oscillators accessible to TESS and, consequently, among the most observationally valuable targets for future high-precision photometric and spectroscopic studies. Their brightness enables higher signal-to-noise ratios, improved mode detection to adapted instruments, and facilitates complementary ground-based follow-up, making them benchmark objects for asteroseismology and exoplanet characterisation. The analysis was performed by combining multiple observing cadences, calibrations, and independent mode-fitting pipelines to ensure robust and consistent results. For the remaining three stars, only the background parameters are reported. From the extracted mode frequencies, we quantified key seismic diagnostics, including the large and small frequency separations ($\Delta\nu$, $\delta\nu_{0,1}$, $\delta\nu_{0,2}$), the asymptotic phase term ε, as well as mode amplitudes and linewidths. Mixed modes were carefully identified in SG stars, providing insight into their internal structure. Detailed forward modelling of the frequencies will be addressed in a future study. Our analysis provides several new insights:

1. The échelle diagrams and modelled power spectral density (PSD) plots are provided for all 29 stars, along with the corresponding lists of extracted mode frequencies.
2. The mode frequencies extracted for σ Dra confirm the results of Hon et al. (2024), which were obtained using a smaller number of TESS sectors. This star represents one of the coolest MS solar-like stars for which individual oscillation modes have been characterised with TESS, thereby extending the parameter space accessible to asteroseismic studies. Only three other stars in a similar effective temperature range are reported in the *Kepler* LEGACY catalogue (Lund et al. 2017). Studying such low-$T_{\rm eff}$ stars is particularly important for exoplanet science: their smaller radii and masses enhance transit and radial velocity signals, enabling more

precise detection and characterisation of Earth-sized planets. Additionally, their close-in habitable zones allow more frequent transits, facilitating follow-up observations. Characterising cooler stars seismically provides a critical foundation for understanding the occurrence and properties of potentially habitable planets.

3. A careful and comparative identification of mixed modes across multiple pipelines is provided, quantifying discrepancies and showing that stars with numerous mixed modes are more evolved. Our work demonstrates the sensitivity of mode identification to pipeline methodology and highlights the need for robust approaches when analysing stars near the main-sequence turn-off. This issue is compounded when modelling the detected mixed modes, as the radial sensitivity of a mode can vary rapidly compared to the frequency differences between stellar models, making detailed seismic modelling particularly challenging (e.g. Fellay et al. 2021).
4. At least eight stars with double-humped or plateau-like p-mode envelopes were identified, including slightly evolved SG and hotter MS stars. This feature, previously reported only in a few *Kepler* and CoRoT targets, is now observed in TESS data, opening new avenues to study the physical processes shaping envelope morphology.
5. Comparison with *Kepler* observations for 16 Cyg A and θ Cyg demonstrates that TESS can reliably recover mode frequencies, even for stars with low SNR or broad F-type modes, while identifying limitations in mode width determination. This emphasises the potential of TESS for expanding the sample of stars with detailed seismic characterisation and identifies prime candidates for future PLATO observations.

Our results confirm that TESS can provide reliable individual mode frequencies for a broad range of solar-like stars, including F-type MS stars and stars with low SNR, enabling studies of stellar interiors across different evolutionary stages. The observed diversity in mode amplitudes, linewidths, and small separations underscores the importance of combining multiple pipelines and careful mode identification to capture both surface and core properties. Future missions such as PLATO, with higher photometric precision and longer time series, will further improve constraints on mode damping, mixed modes, and stellar interiors, thereby advancing our understanding of stellar structure and evolution.

Acknowledgements. This paper includes data collected with the TESS mission, obtained from the MAST data archive at the Space Telescope Science Institute (STScI). Funding for the TESS mission is provided by the NASA Explorer Program. STScI is operated by the Association of Universities for Research in Astronomy, Inc., under NASA contract NAS 5–26555. EP, RAG, BL, LD, JG, ARGS, and DBP acknowledge the support from the GOLF and PLATO Centre National D'Études Spatiales grants. SNB and EC acknowledge support from PLATO ASI-INAF agreement no. 2022-28-HH.0 "PLATO Fase D". EC is funded by the European Union NextGenerationEU RRF M4C2 1.1 No. 2022HY2NSX, "CHRONOS: adjusting the clock(s) to unveil the CHRONOchemo-dynamical Structure of the Galaxy" (PI:S.Cassisi). GTH acknowledges the support of the Science and Technology Facilities Council. MNL acknowledges support from the ESA PRODEX programme (PEA 4000142995). SM acknowledges support from the Spanish Ministry of Science and Innovation with the grant no. PID2023-149439NB-C41. *Softwares*: `emcee` (Foreman-Mackey et al. 2013), `lmfit` (Newville et al. 2025), Matplotlib (Hunter 2007), NumPy (van der Walt et al. 2011), SciPy (Jones et al. 2001), pandas (McKinney 2010; The pandas development team 2024). Some portions of the text were revised with the help of OpenAI's ChatGPT (GPT-4), used for improving clarity and scientific language.

References

Aguilera-Gómez, C., Ramírez, I., & Chanamé, J. 2018, A&A, 614, A55
Anderson, E. R., Duvall, T. L., & Jefferies, S. M. 1990, ApJ, 364, 699
Appourchaux, T. 2020, A&A, 642, A226
Appourchaux, T., Benomar, O., Gruberbauer, M., et al. 2012a, A&A, 537, A134
Appourchaux, T., Chaplin, W. J., García, R. A., et al. 2012b, A&A, 543, A54
Beck, P. G., Bedding, T. R., Mosser, B., et al. 2011, Science, 332, 205
Bedding, T. R., Kjeldsen, H., Bouchy, F., et al. 2005, A&A, 432, L43
Belkacem, K., Dupret, M. A., Baudin, F., et al. 2012, A&A, 540, L7
Belkacem, K., Samadi, R., Goupil, M. J., & Dupret, M. A. 2008, A&A, 478, 163
Bellinger, E. P., Basu, S., Hekker, S., Christensen-Dalsgaard, J., & Ball, W. H. 2021, ApJ, 915, 100
Benomar, O., Bedding, T. R., Mosser, B., et al. 2013, ApJ, 767, 158
Breton, S. N., Dhouib, H., García, R. A., et al. 2023, A&A, 679, A104
Breton, S. N., García, R. A., Ballot, J., Delsanti, V., & Salabert, D. 2022, A&A, 663, A118
Buchele, L., Bellinger, E. P., Hekker, S., & Basu, S. 2025, ApJ, 989, 158
Buldgen, G., Fellay, L., Bétrisey, J., et al. 2024, A&A, 689, A307
Campante, T. L., Handberg, R., Mathur, S., et al. 2011, A&A, 534, A6
Casagrande, L., Schönrich, R., Asplund, M., et al. 2011, A&A, 530, A138
Chontos, A., Huber, D., Sayeed, M., & Yamsiri, P. 2022, JOSS, 7, 3331
Compton, D. L., Bedding, T. R., & Stello, D. 2019, MNRAS, 485, 560
Corsaro, E. & De Ridder, J. 2014, A&A, 571, A71
Corsaro, E., McKeever, J. M., & Kuszlewicz, J. S. 2020, A&A, 640, A130
Davies, G. R., Chaplin, W. J., Farr, W. M., et al. 2015, MNRAS, 446, 2959
Deheuvels, S., Ballot, J., Eggenberger, P., et al. 2020, A&A, 641, A117
Deheuvels, S., Doğan, G., Goupil, M. J., et al. 2014, A&A, 564, A27
Deheuvels, S. & Michel, E. 2010, Astrophys. Space Sci., 328, 259
Deheuvels, S. & Michel, E. 2011, A&A, 535, A91
Desort, M., Lagrange, A.-M., Galland, F., et al. 2009, A&A, 506, 1469
Fellay, L., Buldgen, G., Eggenberger, P., et al. 2021, A&A, 654, A133
Foreman-Mackey, D., Hogg, D. W., Lang, D., & Goodman, J. 2013, PASP, 125, 306
García, R. A. & Ballot, J. 2019, Living Rev. Sol. Phys., 16, 4
García, R. A., Mathur, S., Salabert, D., et al. 2010, Science, 329, 1032
García Saravia Ortiz de Montellano, A., Hekker, S., & Themeßl, N. 2018, MNRAS, 476, 1470
Goldreich, P. & Keeley, D. A. 1977, ApJ, 211, 934
Gould, B. A. 1855, ApJ, 4, 81
Guzik, J. A., Houdek, G., Chaplin, W. J., et al. 2016, ApJ, 831, 17
Handberg, R., Brogaard, K., Miglio, A., et al. 2017, MNRAS, 472, 979
Handberg, R. & Lund, M. N. 2014, MNRAS, 445, 2698
Harvey, J. 1985, Future Missions in Solar, Heliospheric & Space Plasma Physics, 235, 199
Hon, M., Huber, D., Li, Y., et al. 2024, The Astrophysical Journal, 975, 147
Hookway, G. T., Nielsen, M. B., Davies, G. R., et al. 2025, MNRAS, 544, 3247
Houdek, G., Lund, M. N., Trampedach, R., et al. 2019, MNRAS, 487, 595
Huber, D., Bedding, T. R., Stello, D., et al. 2011, ApJ, 743, 143
Huber, D., White, T. R., Metcalfe, T. S., et al. 2022, ApJ, 163, 79
Hunter, J. D. 2007, CiSE, 9, 90
Jones, E., Oliphant, T., & Peterson, P. 2001
Kallinger, T. 2019, arXiv e-prints, arXiv:1906.09428
Kjeldsen, H. & Bedding, T. R. 1995, A&A, 293, 87
Koleva, M. & Vazdekis, A. 2012, A&A, 538, A143
Lomb, N. R. 1976, Astrophys. Space Sci., 39, 447
Lund, M. N., Chontos, A., Grundahl, F., et al. 2025, A&A, 701, A285
Lund, M. N., Handberg, R., Davies, G. R., Chaplin, W. J., & Jones, C. D. 2015, ApJ, 806, 30
Lund, M. N., Silva Aguirre, V., Davies, G. R., et al. 2017, ApJ, 835, 172
Mathur, S., García, R. A., Régulo, C., et al. 2010, A&A, 511, A46
Mathur, S., Handberg, R., Campante, T. L., et al. 2011, ApJ, 733, 95
Mazumdar, A., Monteiro, M. J. P. F. G., Ballot, J., et al. 2014, ApJ, 782, 18
McKinney, W. 2010, scipy
Metcalfe, T. S., Chaplin, W. J., Appourchaux, T., et al. 2012, ApJ, 748, L10
Metcalfe, T. S., Monteiro, M. J. P. F. G., Thompson, M. J., et al. 2010, ApJ, 723, 1583
Mosser, B., Belkacem, K., Goupil, M. J., et al. 2011, A&A, 525, L9
Muterspaugh, M. W., Lane, B. F., Kulkarni, S. R., et al. 2010, ApJ, 140, 1657
Nascimbeni, V., Piotto, G., Börner, A., et al. 2022, A&A, 658, A31
Nascimbeni, V., Piotto, G., Cabrera, J., et al. 2025, A&A, 694, A313
Newville, M., Otten, R., Nelson, A., et al. 2025, LMFIT: Non-Linear Least-Squares Minimization and Curve-Fitting for Python, Zenodo
Nielsen, M. B., Davies, G. R., Ball, W. H., et al. 2021, ApJ, 161, 62
Nielsen, M. B., Ong, J. M. J., Hatt, E. J., et al. 2025, ApJ, 169, 322
Ong, J. M. J. & Basu, S. 2020, ApJ, 898, 127
Ong, J. M. J. & Gehan, C. 2023, ApJ, 946, 92
Ong, J. M. J., Lindsay, C. J., Reyes, C., Stello, D., & Roxburgh, I. W. 2025, ApJ, 980, 199
Peirce, B. 1852, ApJ, 2, 161
Perdelwitz, V., Trifonov, T., Teklu, J. T., Sreenivas, K. R., & Tal-Or, L. 2024, A&A, 683, A125
Rauer, H., Aerts, C., Cabrera, J., et al. 2025, Exp. Astron., 59, 26
Régulo, C., García, R. A., & Ballot, J. 2016, A&A, 589, A103
Ricker, G. R., Winn, J. N., Vanderspek, R., et al. 2014, Proceedings of the SPIE, 9143, 914320
Samadi, R. & Goupil, M. J. 2001, A&A, 370, 136
Santos, A. R. G., Campante, T. L., Chaplin, W. J., et al. 2019, ApJ, 883, 65
Scargle, J. D. 1982, ApJ, 263, 835
Shibahashi, H. 1979, PASJ, 31, 87
Soubiran, C., Brouillet, N., & Casamiquela, L. 2022, A&A, 663, A4
Soubiran, C., Creevey, O. L., Lagarde, N., et al. 2024, A&A, 682, A145
Speagle, J. S. 2020, MNRAS, 493, 3132
Tassoul, M. 1980, ApJS, 43, 469
The pandas development team. 2024, Pandas-Dev/Pandas: Pandas, Zenodo
Themeßl, N., Hekker, S., Southworth, J., et al. 2018, MNRAS, 478, 4669
van der Walt, S., Colbert, S. C., & Varoquaux, G. 2011, CiSE, 13, 22
White, T. R., Bedding, T. R., Gruberbauer, M., et al. 2012, ApJL, 751, L36
White, T. R., Bedding, T. R., Stello, D., et al. 2011, ApJ, 743, 161

Appendix A: Mode identification

The identification of oscillation modes is a crucial step in asteroseismic analyses, as it establishes the link between observed spectral features and their physical interpretation. Accurate mode identification enables the assignment of angular degree and radial order to individual oscillation modes, which is essential for subsequent seismic modelling and inference of stellar properties. Depending on the evolutionary stage and oscillation characteristics of the star, different strategies may be required to reliably identify modes, particularly in the presence of mixed modes, broadened linewidths, or overlapping ridges in the power spectrum.

A.1. Pure p modes

For MS stars with clearly resolved ridges in the power spectrum, all pipelines adopt the standard asymptotic expression (e.g., Tassoul 1980; Mosser et al. 2011; Lund et al. 2017; Breton et al. 2022). The frequencies of $\ell = 0$ and $\ell = 2$ modes are given by

$$\nu_{\mathrm{p}_{n,\ell}} = \left[n + \frac{\ell}{2} + \varepsilon + \frac{\alpha}{2}\left(n - \frac{\nu_{\max}}{\Delta\nu}\right)^2 \right] \Delta\nu - \delta\nu_{0,\ell}\,, \quad \text{(A.1)}$$

where n and ℓ denote the radial order and angular degree, ε is the phase offset, $\delta\nu_{0,\ell}$ the small separation, and α accounts for the curvature of the large separation. Global seismic parameters $\Delta\nu$ and $\nu_{\max}$ are first measured from the power spectrum, then predicted mode frequencies are generated from Eq. (A.1). In this scheme, quadrupole modes are offset from radial modes by $\delta\nu_{0,2}$:

$$\nu_{n_\mathrm{p}-1,2} = \nu_{n_\mathrm{p},0} - \delta\nu_{0,2}\,. \quad \text{(A.2)}$$

and dipole ($\ell = 1$) modes, when not mixed, are offset by

$$\nu_{n_\mathrm{p},1} = \nu_{n_\mathrm{p},0} - \delta\nu_{0,1} + \frac{\Delta\nu}{2}\,. \quad \text{(A.3)}$$

Observed peaks are then matched to the nearest predicted frequencies (Corsaro & De Ridder 2014; Corsaro et al. 2020; Nielsen et al. 2021, 2025; Breton et al. 2022), and modes are labelled according to their angular degree. This approach works well for stars with narrow, regular ridges but becomes challenging for mixed modes, F-like stars, or stars with broad linewidths, where ridge distortion and mode blending can obscure the asymptotic pattern.

A.2. Mixed-mode formulation

For stars exhibiting signatures of mode coupling, particularly dipole mixed modes, mode identification requires a formalism that accounts for the interaction between the *p*- and *g*- mode cavities. In this formulation, pure pressure modes are computed using Eq. (A.1), while pure gravity modes follow Tassoul (1980):

$$\nu_\mathrm{g} = \frac{1}{\Delta\Pi_1\left(n_\mathrm{g} + \frac{1}{2} + \varepsilon_\mathrm{g}\right)}\,, \quad \text{(A.4)}$$

where ε_g is the gravity-mode phase offset and $\Delta\Pi_\ell$ is the asymptotic period spacing. We note that, in the case of sub-giants, the gravity-mode component of mixed modes does not strictly follow the asymptotic regime, as the *g*-mode cavity is relatively small and the mode pattern may deviate significantly from this simple relation (e.g. Ong & Basu 2020). The asymptotic description adopted here should therefore be regarded as an approximation in this evolutionary phase.

Two complementary approaches were applied using `apollinaire` and `PBjam`. For `apollinaire` results, an *a posteriori* mixed mode-identification method was implemented. First, the $\ell = 0$ and $\ell = 2$ modes are identified using the standard asymptotic relation of Eq. (A.1) for pure pressure modes. Remaining significant peaks are provisionally associated with dipole mixed modes, which are then compared to the frequencies predicted by the best-fitting asymptotic mixed-mode model. Peaks that do not correspond to model-predicted modes are treated as noise and excluded. The mixed-mode frequencies are computed by solving the implicit asymptotic relation (Shibahashi 1979):

$$\cot\left(\Theta_\mathrm{g}\right)\tan\left(\Theta_\mathrm{p}\right) = q\,, \quad \text{(A.5)}$$

with phases defined as (Ong & Gehan 2023):

$$\Theta_\mathrm{p} = \frac{\pi}{\Delta\nu}\left(\nu - \nu_\mathrm{p}\right), \quad \text{(A.6)}$$

$$\Theta_\mathrm{g} = \frac{\pi}{2} - \frac{\pi}{\Delta\Pi_\ell}\left(\frac{1}{\nu_\mathrm{g}} - \frac{1}{\nu}\right), \quad \text{(A.7)}$$

where ν_p and ν_g are the closest pure pressure and gravity mode frequencies to ν, respectively. The asymptotic parameters $\Delta\nu$, α, $\delta\nu_{0,1}$, ε, ε_g, q, and $\Delta\Pi_1$ are adjusted within a Bayesian MCMC framework using `emcee`, with a Gaussian log-likelihood:

$$\ln\mathcal{L} = -\frac{1}{2}\sum_{\mathrm{modes}}\frac{(\nu_\mathrm{obs} - \nu_\mathrm{model})^2}{\sigma^2_\mathrm{obs}}\,, \quad \text{(A.8)}$$

where ν_obs are the observed peak-bagged frequencies, ν_model the model frequencies, and σ_obs the observational uncertainties, with the larger of asymmetric bounds adopted conservatively. This procedure allows a clear separation between genuine oscillation modes and spurious noise features. Although the MCMC convergence yields asymptotic parameters describing the oscillation pattern, here it is employed solely as a mode-identification tool.

`PBjam`, in contrast, follows an *a priori* non-asymptotic approach, particularly suited for SG stars with mixed modes. Radial and quadrupole modes are modelled with standard asymptotic relations of Eqs. (A.1) and (A.2), whereas dipole modes are treated as combinations of pure pressure and gravity modes with Eq. (A.4), and described by a non-asymptotic relation (Deheuvels & Michel 2010; Ong & Basu 2020), which explicitly accounts for the coupling strength between the *p*- and *g*-mode cavities (Nielsen et al. 2025).

A.3. Data driven approach

Unlike purely asymptotic approaches, which rely primarily on theoretical mode-spacing relations, the method adopted by FAMED identifies oscillation modes using a data-driven, multistep analysis of the power spectrum. Candidate peaks are first detected through statistical sampling of the spectrum without imposing a fixed asymptotic pattern *a priori*. This allows oscillation modes, including dipole modes affected by mixed-mode behaviour, to be identified based on their significance and spectral morphology rather than their proximity to expected asymptotic locations. Once candidate frequencies are identified, global asteroseismic parameters are refined using asymptotic descriptions of Eqs. (A.1) and (A.2). These well-behaved modes serve as anchors for the oscillation pattern, enabling a clearer separation of dipolemodes from both noise and neighbouring ridges.

For each candidate dipole peak, Bayesian model comparison is employed to assess whether the feature is statistically significant relative to the background and whether it is best described by a single oscillation mode, blended peaks, or more complex structures such as rotational splitting. This step allows genuine mixed dipole modes to be distinguished from spurious detections and noise-driven artifacts. The identification process is iterative, with ambiguous peaks discarded and mode classifications refined based on statistical evidence and consistency with the evolving global pattern. In this framework, dipole mixed modes are identified primarily through their statistical significance and spectral structure, with asymptotic relations applied only at a later stage to refine mode labelling and spacing. This approach enables a robust discrimination between physically meaningful mixed modes and noise-induced features in complex oscillation spectra.

Appendix B: Échelle diagrams

We present here the star-by-star échelle diagram for the reference dataset with observed modes as extracted by the three pipelines used in this work, and the fitted model with `apollinaire`. Stars are listed by increasing $\nu_{\max}$.

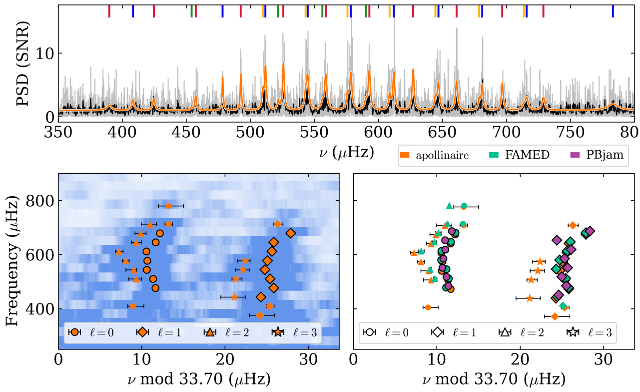

Fig. B.1. Top panel: The Power Spectral Density (PSD) of the reference dataset of TIC 354552931 (HD 36553) is shown in grey, over a frequency range centred on $\nu_{\max}$. Its moving mean (10-point window) is shown in black. The orange curve represents the model fitted by `apollinaire`, with the corresponding frequencies listed in Table C.1. Identified peaks are indicated by vertical coloured lines above the PSD: blue for $\ell = 0$, red for $\ell = 1$, yellow for $\ell = 2$ and green for $\ell = 3$. Bottom panels: The left panel shows an échelle diagram with frequencies fitted by the reference pipeline: circles ($\ell = 0$), diamonds ($\ell = 1$), triangles ($\ell = 2$), and stars ($\ell = 3$). The right panel compares these frequencies with those obtained by the other pipelines, where the markers of each pipeline was slightly vertically shifted within $\Delta\nu$ to improve readability. Markers are the same as in the left panel, with `apollinaire` in orange, FAMED in green, and `PBjam` in violet. Markers with black edges correspond to modes included in the minimal list, while markers without black edges correspond to modes in the maximal list or excluded from any list. For clarity, the échelle diagram has been offset by -5 μHz to improve ridges visibility.

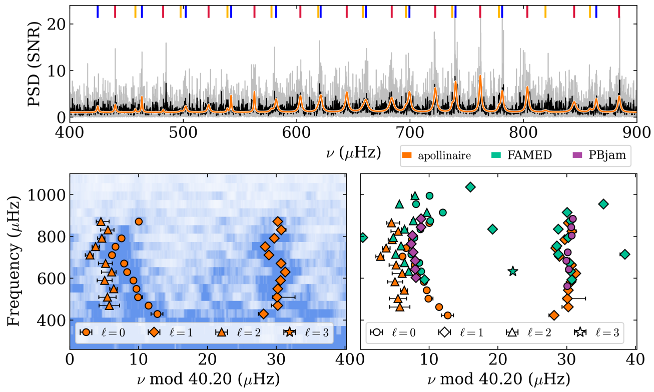

Fig. B.2. Same as Figure B.1, but for TIC 161825882 (θ Dra). The échelle diagram has been offset by 10 μHz to improve ridges visibility. Modes for this star have not been flagged, as the pipelines do not agree on their identification; all are shown with black edges markers.

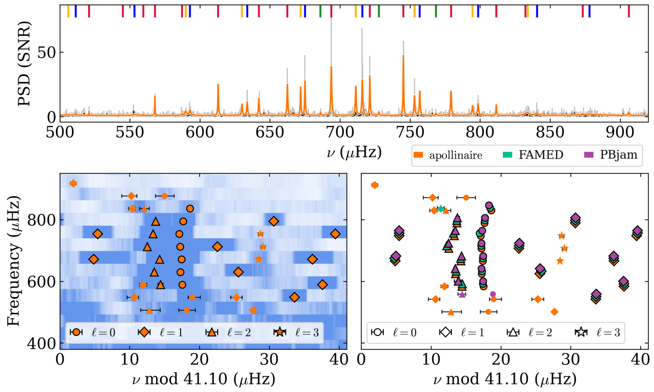

Fig. B.3. Same as Figure B.1, but for TIC 123699670 (HD 62644). The échelle diagram has not been offset.

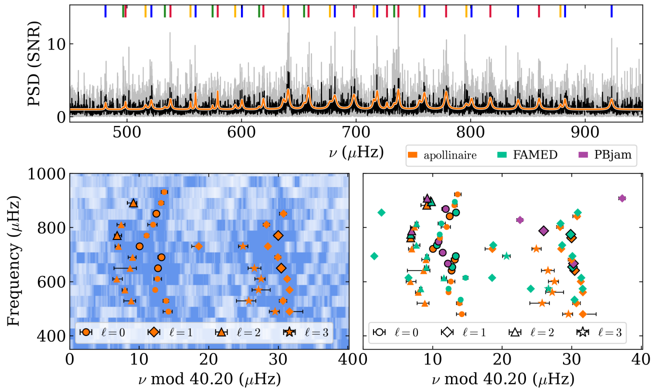

Fig. B.4. Same as Figure B.1, but for TIC 236871353 (68 Dra). The échelle diagram has been offset by 25 μHz to improve ridges visibility.

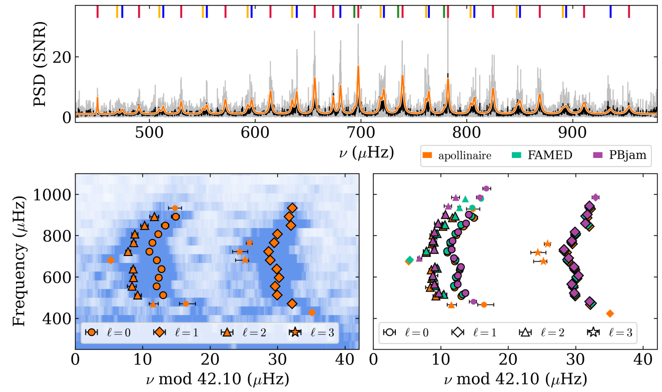

Fig. B.5. Same as Figure B.1, but for TIC 441813918 (35 Dra). The échelle diagram has been offset by -5 μHz to improve ridges visibility.

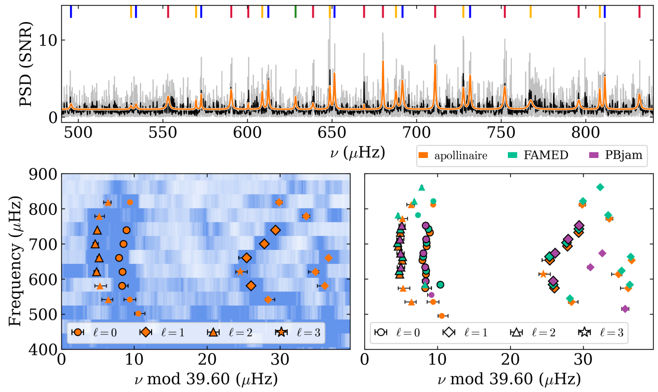

Fig. B.6. Same as Figure B.1, but for TIC 41195655 (27 Cyg). The échelle diagram has been offset by 10 μHz to improve ridges visibility.

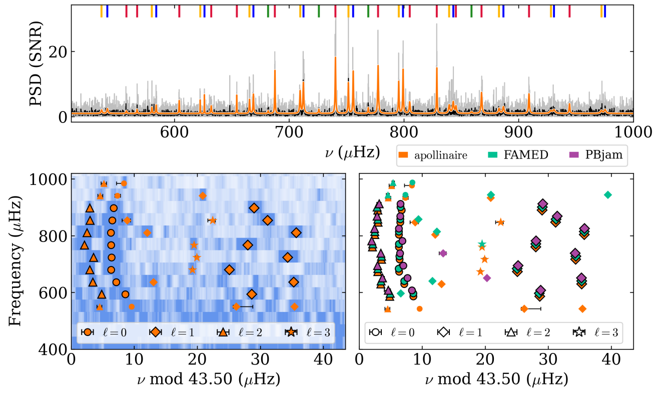

Fig. B.7. Same as Figure B.1, but for TIC 48194330 (HD 175225). The échelle diagram has been offset by 10 μHz to improve ridges visibility.

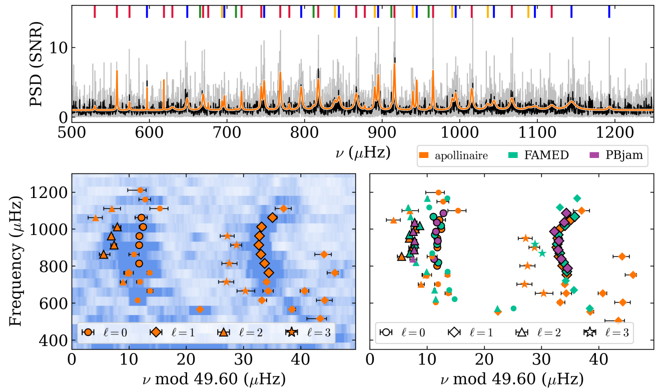

Fig. B.8. Same as Figure B.1, but for TIC 219420836 (ζ Pic). The échelle diagram has been offset by 40 μHz to improve ridges visibility.

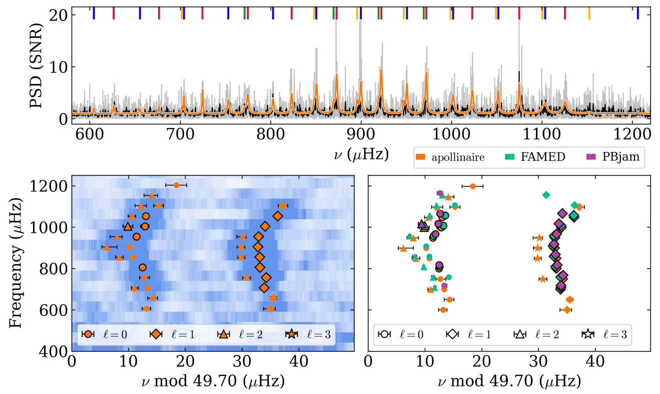

Fig. B.9. Same as Figure B.1, but for TIC 255630992 (HD 46569). The échelle diagram has been offset by -5 μHz to improve ridges visibility.

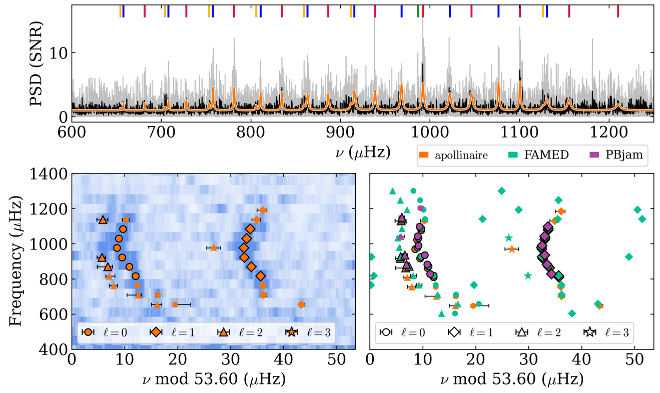

Fig. B.10. Same as Figure B.1, but for TIC 421444084 (υ Cep). The échelle diagram has been offset by -5 μHz to improve ridges visibility.

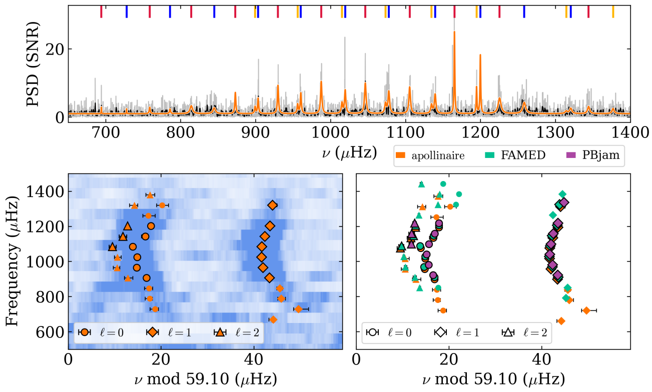

Fig. B.11. Same as Figure B.1, but for TIC 232563914 (HD 136064). The échelle diagram has not been offset.

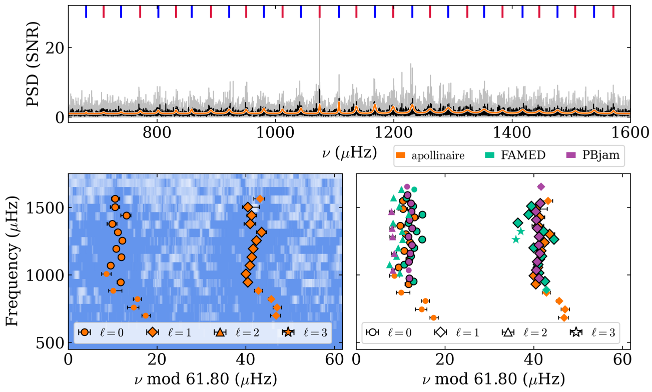

Fig. B.12. Same as Figure B.1, but for TIC 441804568 (ψ^1 Dra A). The échelle diagram has been offset by 5 μHz to improve ridges visibility.

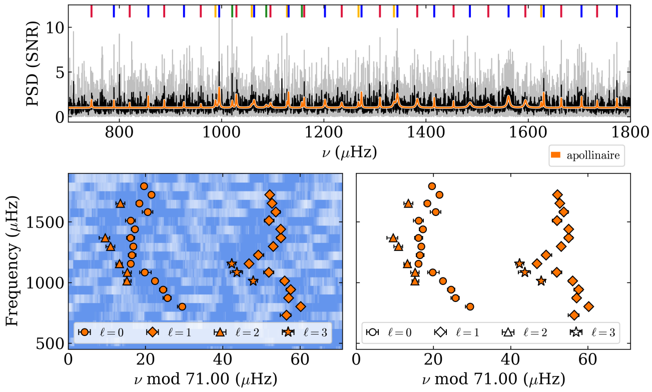

Fig. B.13. Same as Figure B.1, but for TIC 405902259 (HD 191195). The échelle diagram has been offset by 50 μHz to improve ridges visibility.

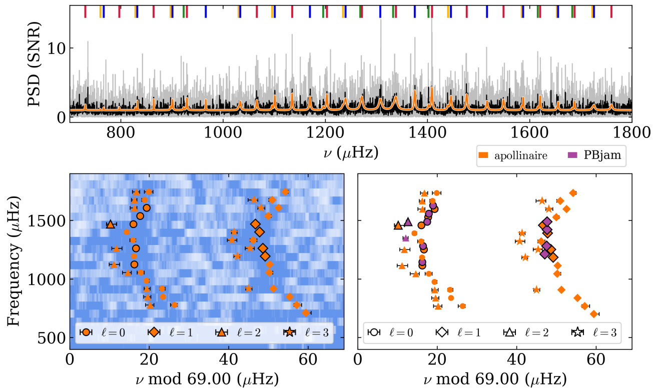

Fig. B.14. Same as Figure B.1, but for TIC 170225363 (HD 50223). The échelle diagram has been offset by 50 μHz to improve ridges visibility.

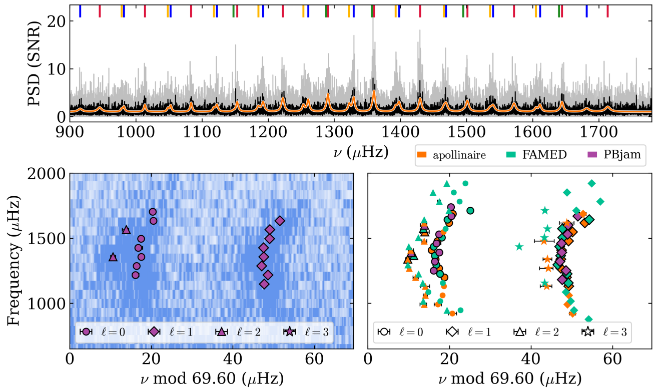

Fig. B.15. Same as Figure B.1, but for TIC 233121747 (36 Dra). The échelle diagram has been offset by 60 μHz to improve ridges visibility.

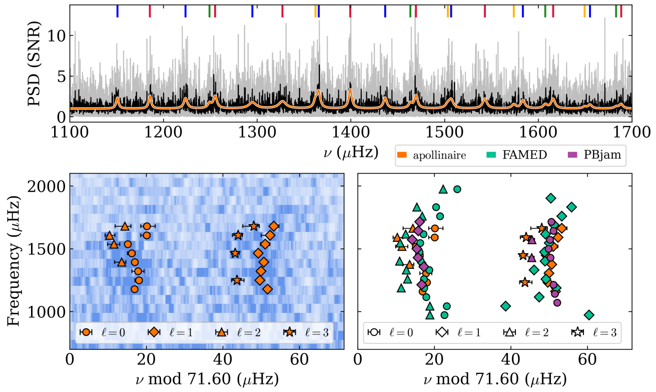

Fig. B.16. Same as Figure B.1, but for TIC 308844962 (HR 3220). The échelle diagram has been offset by 60 μHz to improve ridges visibility. Modes for this star have not been flagged, as the pipelines do not agree on their identification; all are shown with black edges markers.

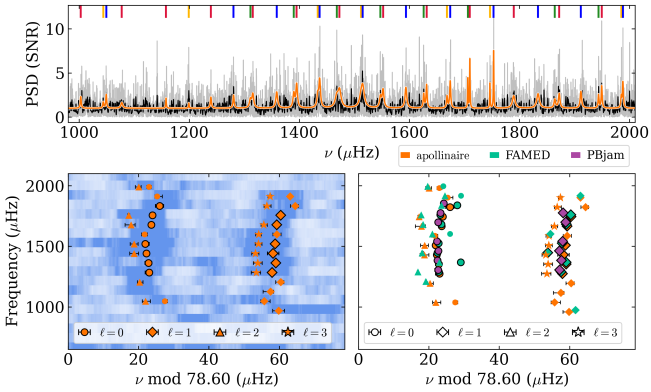

Fig. B.17. Same as Figure B.1, but for TIC 58445695 (17 Cyg). The échelle diagram has not been offset.

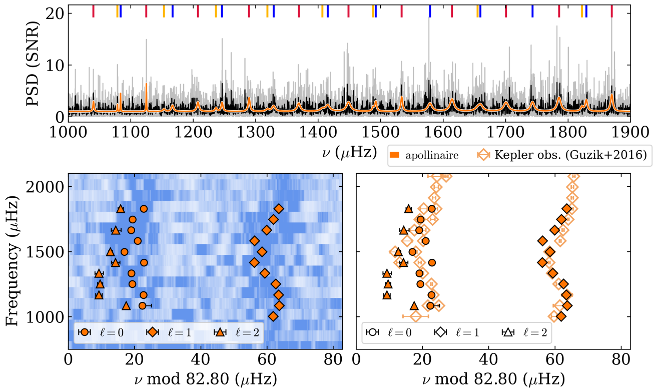

Fig. B.18. Same as Figure B.1, but for TIC 27014182 (θ Cyg). The échelle diagram has been offset by -15 μHz to improve ridges visibility.

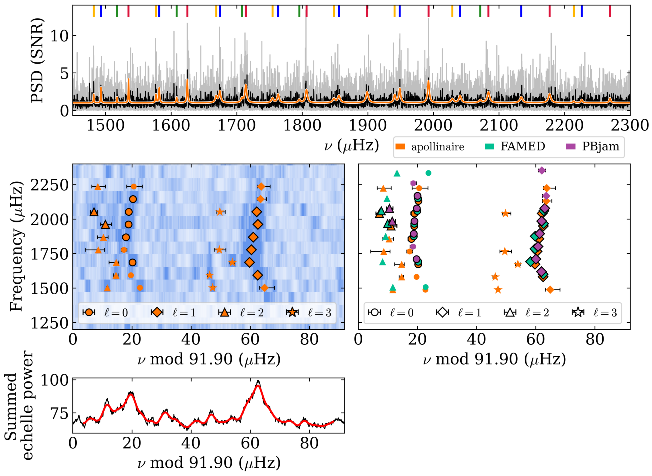

Fig. B.19. Same as Figure B.1, but for TIC 26884478 (HD 184960). The échelle diagram has not been offset. The bottom panel shows the sum of the échelle diagram over frequency as a function of $\Delta\nu$ in black, with its moving mean (window = 1000 points) in red.

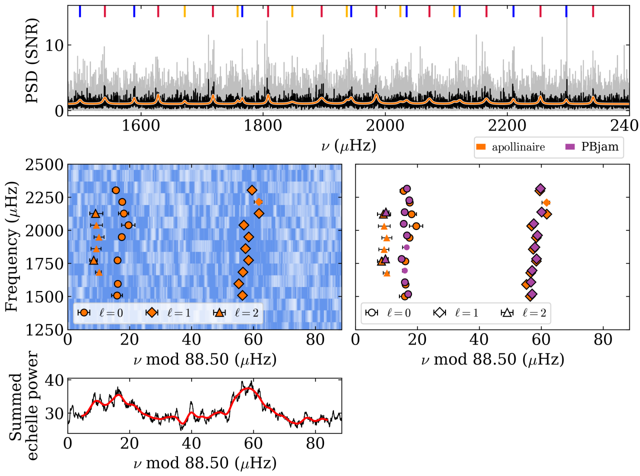

Fig. B.20. Same as Figure B.1, but for TIC 233195546 (ω Dra). The échelle diagram has been offset by -20 μHz to improve ridges visibility. The bottom panel shows the sum of the échelle diagram over frequency as a function of $\Delta\nu$ in black, with its moving mean (window = 2000 points) in red.

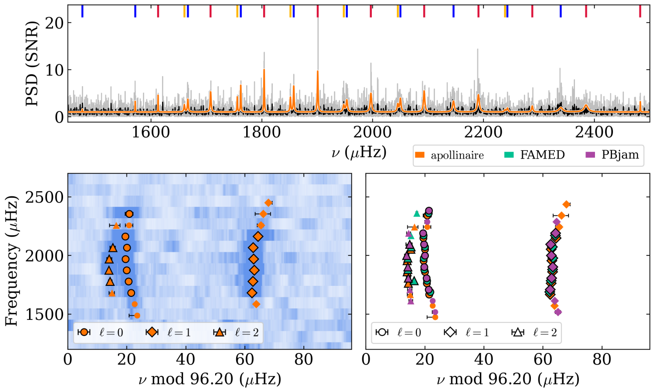

Fig. B.21. Same as Figure B.1, but for TIC 22516402 (99 Her). The échelle diagram has been offset by 10 μHz to improve ridges visibility.

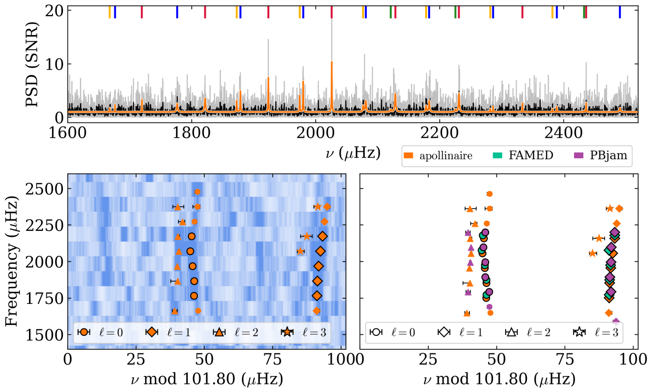

Fig. B.22. Same as Figure B.1, but for TIC 130645536 (HD 53705). The échelle diagram has not been offset.

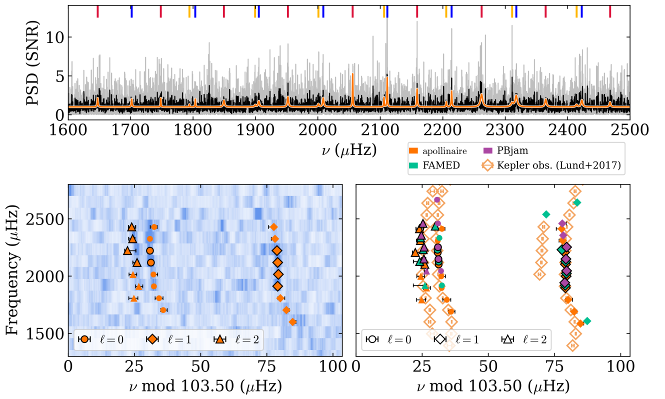

Fig. B.23. Same as Figure B.1, but for TIC 27533341 (16 Cyg A). The échelle diagram has been offset by 10 μHz to improve ridges visibility.

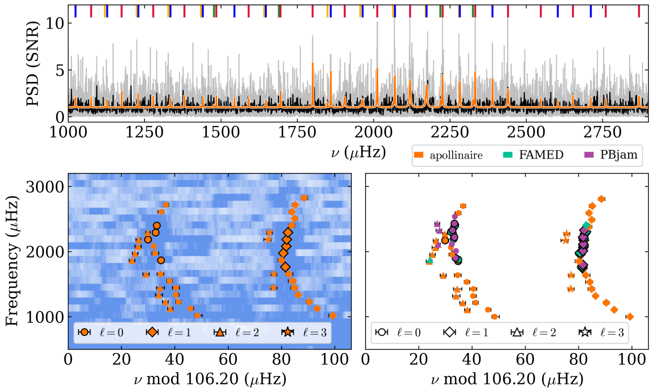

Fig. B.24. Same as Figure B.1, but for TIC 9728611 (72 Her). The échelle diagram has been offset by 20 μHz to improve ridges visibility.

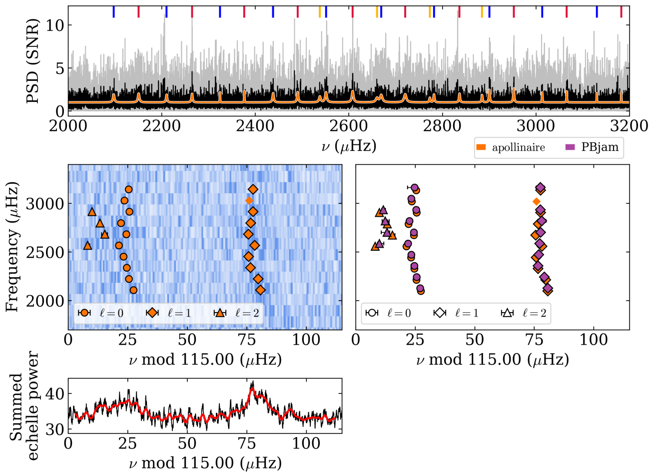

Fig. B.25. Top and middle panels are the same as Figure B.1, but for TIC 289622310 (19 Dra). The échelle diagram has not been offset. The bottom panel shows the sum of the échelle diagram over frequency as a function of Δν in black, with its moving mean (window = 2000 points) in red.

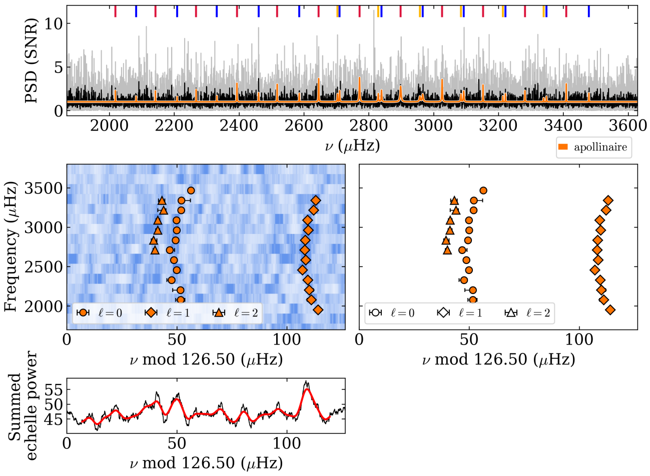

Fig. B.26. Top and middle panels are the same as Figure B.1, but for TIC 20601206 (HD 176051). The échelle diagram has been offset by 7 μHz to improve ridges visibility. The bottom panel shows the sum of the échelle diagram over frequency as a function of Δν in black, with its moving mean (window = 1000 points) in red.

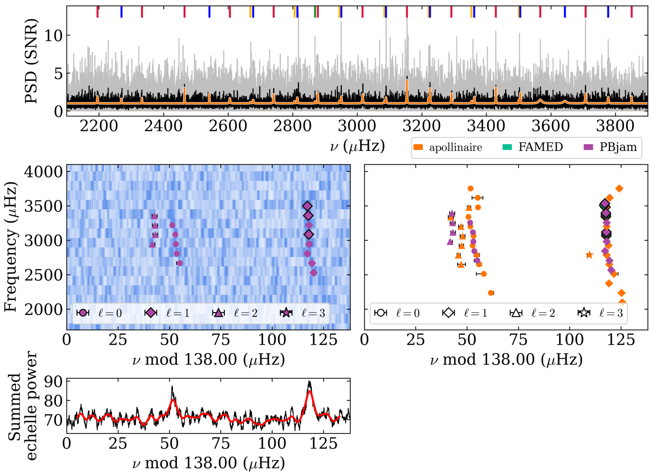

Fig. B.27. Top and middle panels are the same as Figure B.1, but for TIC 403585118 (HD 193664). The échelle diagram has not been offset. The bottom panel shows the sum of the échelle diagram over frequency as a function of Δν in black, with its moving mean (window = 2000 points) in red.

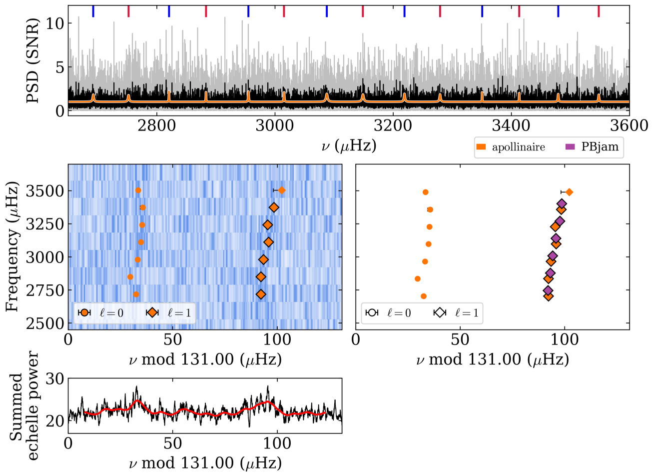

Fig. B.28. Top and middle panels are the same as Figure B.1, but for TIC 219777482 (26 Dra). The échelle diagram has been offset by 40 μHz to improve ridges visibility. The bottom panel shows the sum of the échelle diagram over frequency as a function of $\Delta\nu$ in black, with its moving mean (window = 5000 points) in red.

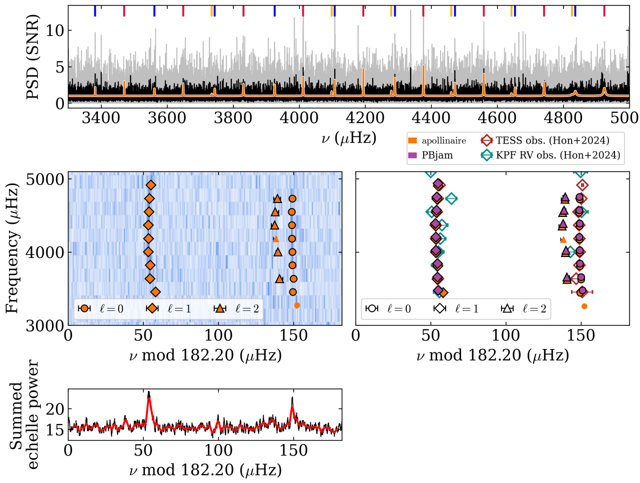

Fig. B.29. Top and middle panels are the same as Figure B.1, but for TIC 259237827 (σ Dra). The échelle diagram has been offset by -50 μHz to improve ridges visibility. The bottom panel shows the sum of the échelle diagram over frequency as a function of $\Delta\nu$ in black, with its moving mean (window = 2000 points) in red.

Appendix C: Frequency tables

We present here the star-by-star resulting mode frequencies obtained from `apollinaire`, FAMED and `PBjam` for the reference dataset. The other tables are available in machine-readable format.

Table C.1. List of oscillation mode frequencies obtained from the reference dataset of TIC 354552931 (HD 36553) using `apollinaire`, FAMED, and `PBjam`. The quoted radial orders (n) are indicative. The flag column indicates whether a given mode is included in the minimal (1) or maximal (2) frequency set, or excluded (3).

n	ℓ	`apollinaire`	FAMED	`PBjam`	flag
10	1	$389.86^{+1.78}_{-1.24}$	–	–	3
11	0	$408.36^{+1.29}_{-0.62}$	–	–	3
11	1	$424.73^{+0.54}_{-0.38}$	$424.54^{+0.08}_{-0.09}$	–	2
11	3	$454.24^{+1.28}_{-1.65}$	–	–	3
12	1	$457.41^{+0.35}_{-0.41}$	$457.57^{+0.18}_{-0.20}$	$457.75^{+0.31}_{-0.17}$	1
13	0	$478.46^{+0.21}_{-0.21}$	$477.92^{+0.11}_{-0.10}$	$478.17^{+0.19}_{-0.18}$	1
13	1	$492.64^{+0.16}_{-0.16}$	$492.62^{+0.07}_{-0.07}$	$492.36^{+0.29}_{-0.34}$	1
13	2	$509.83^{+0.65}_{-0.93}$	$510.27^{+0.23}_{-0.19}$	–	2
14	0	$511.86^{+0.23}_{-0.25}$	$511.95^{+0.12}_{-0.12}$	$511.66^{+0.14}_{-0.15}$	1
13	3	$521.80^{+0.73}_{-0.49}$	–	–	3
14	1	$525.89^{+0.20}_{-0.20}$	$525.99^{+0.25}_{-0.25}$	$525.49^{+0.25}_{-0.22}$	1
14	2	$543.25^{+0.35}_{-0.95}$	$543.42^{+0.17}_{-0.17}$	–	2
15	0	$544.80^{+0.39}_{-0.40}$	$545.36^{+0.22}_{-0.22}$	$544.90^{+0.23}_{-0.22}$	1
14	3	$556.32^{+0.78}_{-0.91}$	–	–	3
15	1	$558.98^{+0.31}_{-0.30}$	$558.53^{+0.10}_{-0.10}$	$559.89^{+0.17}_{-0.20}$	1
15	2	$576.00^{+0.41}_{-0.41}$	–	–	3
16	0	$578.57^{+0.28}_{-0.27}$	$578.41^{+0.16}_{-0.16}$	$578.69^{+0.13}_{-0.18}$	1
15	3	$590.31^{+0.60}_{-0.94}$	–	–	3
16	1	$593.00^{+0.35}_{-0.38}$	$592.64^{+0.34}_{-0.34}$	$593.23^{+0.27}_{-0.29}$	1
16	2	$608.88^{+0.50}_{-0.43}$	$609.72^{+0.37}_{-0.37}$	–	2
17	0	$612.15^{+0.21}_{-0.22}$	$612.14^{+0.16}_{-0.16}$	$612.62^{+0.26}_{-0.29}$	1
17	1	$627.22^{+0.29}_{-0.31}$	$627.28^{+0.13}_{-0.13}$	$627.71^{+0.34}_{-0.20}$	1
17	2	$644.62^{+0.64}_{-0.56}$	$645.00^{+0.29}_{-0.26}$	–	2
18	0	$646.98^{+0.34}_{-0.34}$	$647.00^{+0.22}_{-0.23}$	$646.29^{+0.32}_{-0.30}$	1
18	1	$661.16^{+0.28}_{-0.29}$	$661.33^{+0.08}_{-0.08}$	$659.70^{+0.25}_{-0.38}$	1
18	2	$678.90^{+0.63}_{-0.72}$	$679.18^{+0.35}_{-0.33}$	–	2
19	0	$681.18^{+0.21}_{-0.25}$	$681.25^{+0.18}_{-0.12}$	$680.81^{+0.24}_{-0.32}$	1
19	1	$696.89^{+0.43}_{-0.45}$	$696.90^{+0.18}_{-0.17}$	$697.37^{+0.38}_{-0.36}$	1
19	2	$713.71^{+0.79}_{-1.06}$	$714.01^{+0.12}_{-0.13}$	–	2
20	0	$715.92^{+0.46}_{-0.43}$	$715.85^{+0.14}_{-0.16}$	–	2
20	1	$729.00^{+0.65}_{-0.54}$	–	–	3
21	2	–	$781.61^{+0.09}_{-0.09}$	–	3
22	0	$783.34^{+1.78}_{-1.22}$	$783.37^{+0.10}_{-0.11}$	–	2